Cell

Phase Separation of a PKA Regulatory Subunit Controls cAMP Compartmentation and Oncogenic Signaling

Graphical Abstract

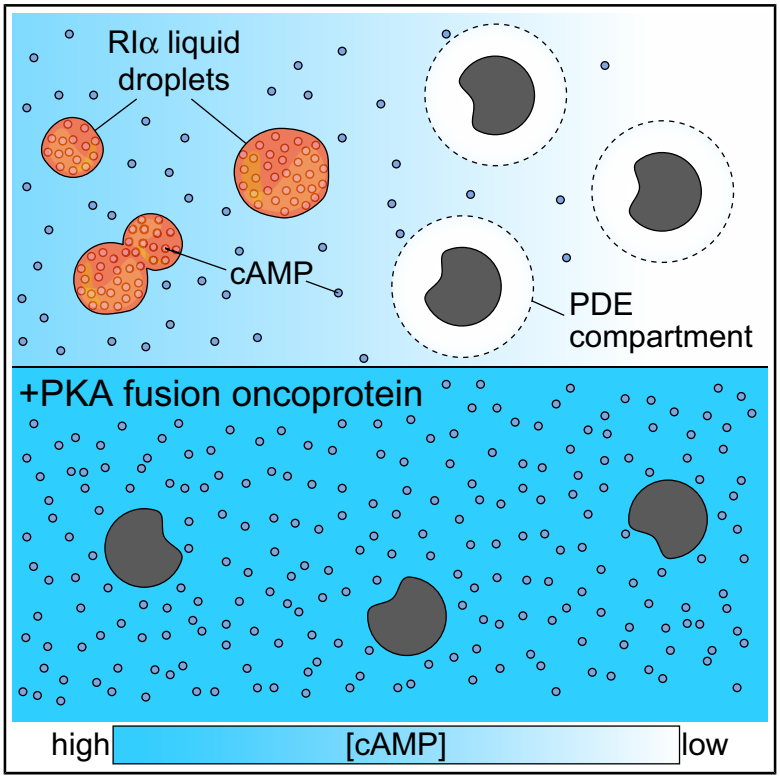

Authors

Jason Z. Zhang, Tsan-Wen Lu, Lucas M. Stolerman, ..., Susan S. Taylor, Sohum Mehta, Jin Zhang

Correspondence

jzhang32@ucsd.edu

In Brief

cAMP-responsive condensate formation by PKA's RIα subunit controls local signaling, and disruption of phase separation in this context contributes to tumorigenesis.

Highlights

- PKA RIα undergoes liquid-liquid phase separation in response to cAMP dynamics
- RIα condensates dynamically sequester cAMP and retain high PKA activity
- RIα phase separation is necessary for effective cAMP compartmentation
- A PKA oncoprotein disrupts RIα bodies, leading to aberrant signaling and growth

Zhang et al., 2020, Cell *182*, 1531–1544
September 17, 2020
https://doi.org/10.1016/j.cell.2020.07.043

CellPress

Cell

CellPress

Article

Phase Separation of a PKA Regulatory Subunit Controls cAMP Compartmentation and Oncogenic Signaling

Jason Z. Zhang,[1,2] Tsan-Wen Lu,[3] Lucas M. Stolerman,[4] Brian Tenner,[1] Jessica R. Yang,[5] Jin-Fan Zhang,[1,2] Martin Falcke,[6,7] Padmini Rangamani,[4] Susan S. Taylor,[1,3] Sohum Mehta,[1] and Jin Zhang[1,2,3,5,8,*]

[1]Department of Pharmacology, University of California, San Diego, La Jolla, CA 92093, USA
[2]Department of Bioengineering, University of California, San Diego, La Jolla, CA 92093, USA
[3]Department of Chemistry and Biochemistry, University of California, San Diego, La Jolla, CA 92093, USA
[4]Department of Mechanical and Aerospace Engineering, University of California, San Diego, La Jolla, CA 92093, USA
[5]Department of Pharmacology and Molecular Sciences, The Johns Hopkins University School of Medicine, Baltimore, MD 21205, USA
[6]Mathematical Cell Physiology, Max Delbrück Center for Molecular Medicine, 13125 Berlin, Germany
[7]Department of Physics, Humboldt University, 12489 Berlin, Germany
[8]Lead Contact
*Correspondence: jzhang32@ucsd.edu
https://doi.org/10.1016/j.cell.2020.07.043

SUMMARY

The fidelity of intracellular signaling hinges on the organization of dynamic activity architectures. Spatial compartmentation was first proposed over 30 years ago to explain how diverse G protein-coupled receptors achieve specificity despite converging on a ubiquitous messenger, cyclic adenosine monophosphate (cAMP). However, the mechanisms responsible for spatially constraining this diffusible messenger remain elusive. Here, we reveal that the type I regulatory subunit of cAMP-dependent protein kinase (PKA), RIα, undergoes liquid-liquid phase separation (LLPS) as a function of cAMP signaling to form biomolecular condensates enriched in cAMP and PKA activity, critical for effective cAMP compartmentation. We further show that a PKA fusion oncoprotein associated with an atypical liver cancer potently blocks RIα LLPS and induces aberrant cAMP signaling. Loss of RIα LLPS in normal cells increases cell proliferation and induces cell transformation. Our work reveals LLPS as a principal organizer of signaling compartments and highlights the pathological consequences of dysregulating this activity architecture.

INTRODUCTION

3′,5′-cyclic adenosine monophosphate (cAMP) is a universal regulator of cellular function and behavior across evolution. In eukaryotes, cAMP production is canonically triggered in response to hormone signaling via G protein-coupled receptor (GPCR)-mediated activation of transmembrane adenylyl cyclases (ACs), which catalyze synthesis of cAMP from ATP. cAMP signals are transduced by a number of well-studied effector proteins, most prominently cAMP-dependent protein kinase (PKA), a tetrameric holoenzyme consisting of a regulatory subunit dimer bound to a pair of catalytic subunits. Binding of cAMP to the PKA regulatory subunit unleashes the activity of the PKA catalytic subunit (PKA_{cat}), which then phosphorylates a myriad of targets throughout the cell. Together, cAMP and PKA exert tight control over numerous physiological processes, from cell growth and survival (Gottesman and Fleischmann, 1986; Jhala et al., 2003; Li et al., 2000) to cardiac (Boularan and Gales, 2015) and neuronal (Kandel, 2012) functions.

The functional diversity of cAMP signaling is driven by hundreds of GPCR inputs (Kroeze et al., 2003) capable of elevating cAMP levels to produce distinct cellular responses (Patra and Brady, 2018). This remarkable specificity may be achieved through compartmentation of cAMP, a concept first proposed over 35 years ago (Brunton et al., 1981; Buxton and Brunton, 1983; Steinberg and Brunton, 2001). Indeed, cAMP gradients (Bacskai et al., 1993; Gorshkov et al., 2017; Lim et al., 2008; Nikolaev et al., 2006) and microdomains (Maiellaro et al., 2016; Terrin et al., 2012; Zaccolo and Pozzan, 2002) have been observed experimentally in various contexts. Although compartmentalized AC activity is involved in forming these cAMP microdomains (Cooper, 2003; Willoughby and Cooper, 2007), cAMP-hydrolyzing phosphodiesterases (PDEs) are widely considered the primary diffusional barrier responsible for fencing local cAMP pools (Baillie, 2009; Houslay, 2010; Zaccolo, 2006).

However, this long-standing model of PDE-controlled cAMP compartmentation is at odds with reports describing almost unrestricted (e.g., 270–780 $\mu m^2/s$) cAMP diffusion in cells (Bacskai et al., 1993; Chen et al., 1999; Nikolaev et al., 2004). Indeed,

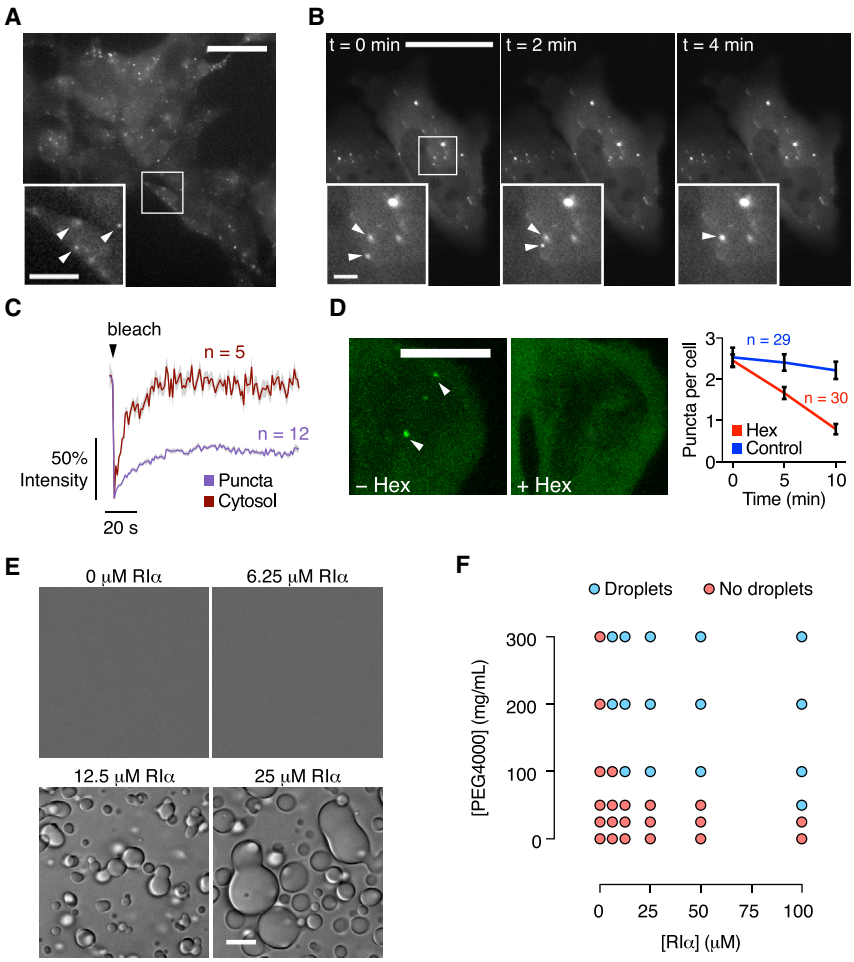

Figure 1. The Endogenous PKA Regulatory Subunit RIα Undergoes Phase Separation

(A) Observing the localization of endogenously expressed RIα. The 11th β strand of GFP (FP_{11}) was knocked in at the C terminus of RIα in HEK293A cells. Transfecting these 293-RIα cells with the remaining GFP β strands ($GFP_{1–10}$) and imaging them in the GFP channel revealed formation of fluorescent RIα puncta.

(B) Representative GFP fluorescence images of 293-RIα cells transfected with $GFP_{1–10}$ show merging of endogenous RIα puncta.

(C) Monitoring the dynamics of labeled RIα. FRAP of RIα puncta (blue curve) compared with diffuse RIα (red curve) in $GFP_{1–10}$-transfected 293-RIα cells. Curves show the average time course of normalized fluorescence intensity. Solid lines indicate the mean and shaded areas indicate SEM.

(D) RIα punctum disruption by 1,6-hexanediol. Representative GFP fluorescence images of $GFP_{1–10}$-transfected 293-RIα cells before (t = 0 min, left) and after (t = 10 min, center) 2.5% 1,6-hexanediol addition. Quantification of the number of RIα puncta per cell at the indicated times with (Hex, red curve) or without (control, blue curve) 1,6-hexanediol addition. Error bars indicate ± SEM.

(E) Representative differential interference contrast (DIC) images showing liquid droplet formation by purified RIα at the indicated concentrations *in vitro*.

(F) Representative *in vitro* phase diagram of RIα liquid droplet formation at varying concentrations of PEG 4000. Each condition was assessed at least twice.

Scale bars are as follows: (A) 30 μm (inset, 10 μm), (B) 30 μm (inset, 1 μm), (D) 10 μm, (E) 10 μm.

various computational studies have failed to reproduce formation of cAMP gradients through the sole action of PDEs (Boras et al., 2014; Lohse et al., 2017; Rich et al., 2000, 2001; Saucerman et al., 2014), whose catalytic activity appears to be insufficient to constrain such a rapidly diffusing messenger (Boras et al., 2014; Lohse et al., 2017), suggesting that experimentally observed cAMP microdomains instead require substantially (~100- to 10,000-fold) slower cAMP diffusion. Notably, more recent investigations have reported significantly lower cytosolic cAMP diffusion rates that are more conducive for cAMP compartmentalization than the original estimates (Agarwal et al., 2016; Richards et al., 2016). However, the specific mechanisms responsible for spatially constraining this critical second messenger remain to be elucidated.

Here we identify the formation of biomolecular condensates of the type I regulatory subunit of PKA, RIα, as a key driver of cAMP compartmentation. RIα undergoes liquid-liquid phase separation (LLPS) at endogenous levels as a function of dynamic cAMP signaling to form RIα bodies harboring high levels of cAMP and PKA activity, and this dynamic cAMP sequestration is required to spatially constrain cAMP in cells. Importantly, RIα LLPS is explicitly disrupted by a PKA_{cat} fusion oncoprotein present in the atypical liver cancer fibrolamellar carcinoma (FLC) (Honeyman et al., 2014), leading to aberrant cAMP signaling and cell transformation. Our work reveals LLPS as an essential coordinator of signaling compartments and provides critical mechanistic clues into the etiology of FLC, highlighting the pathological consequences of dysregulated signaling activity architecture.

RESULTS

RIα Undergoes LLPS at Endogenous Levels

Of the four non-redundant PKA regulatory subunits, only RIα is ubiquitously expressed, and it is essential for proper regulation of PKA activity (Cadd and McKnight, 1989). To visualize the dynamics of RIα expressed at endogenous levels, we introduced the 11th β strand of GFP (FP_{11}) (Leonetti et al., 2016) at the C terminus of RIα via CRISPR-Cas9 in HEK293A cells, yielding the 293-RIα cell line. This small segment permits efficient knockin and enables targeted reconstitution of intact GFP when the remainder of superfolder GFP ($GFP_{1–10}$) is co-expressed. By doing so in 293-RIα cells, we observed fluorescent puncta (Figure 1A) similar to those seen with overexpressed RIα (Day

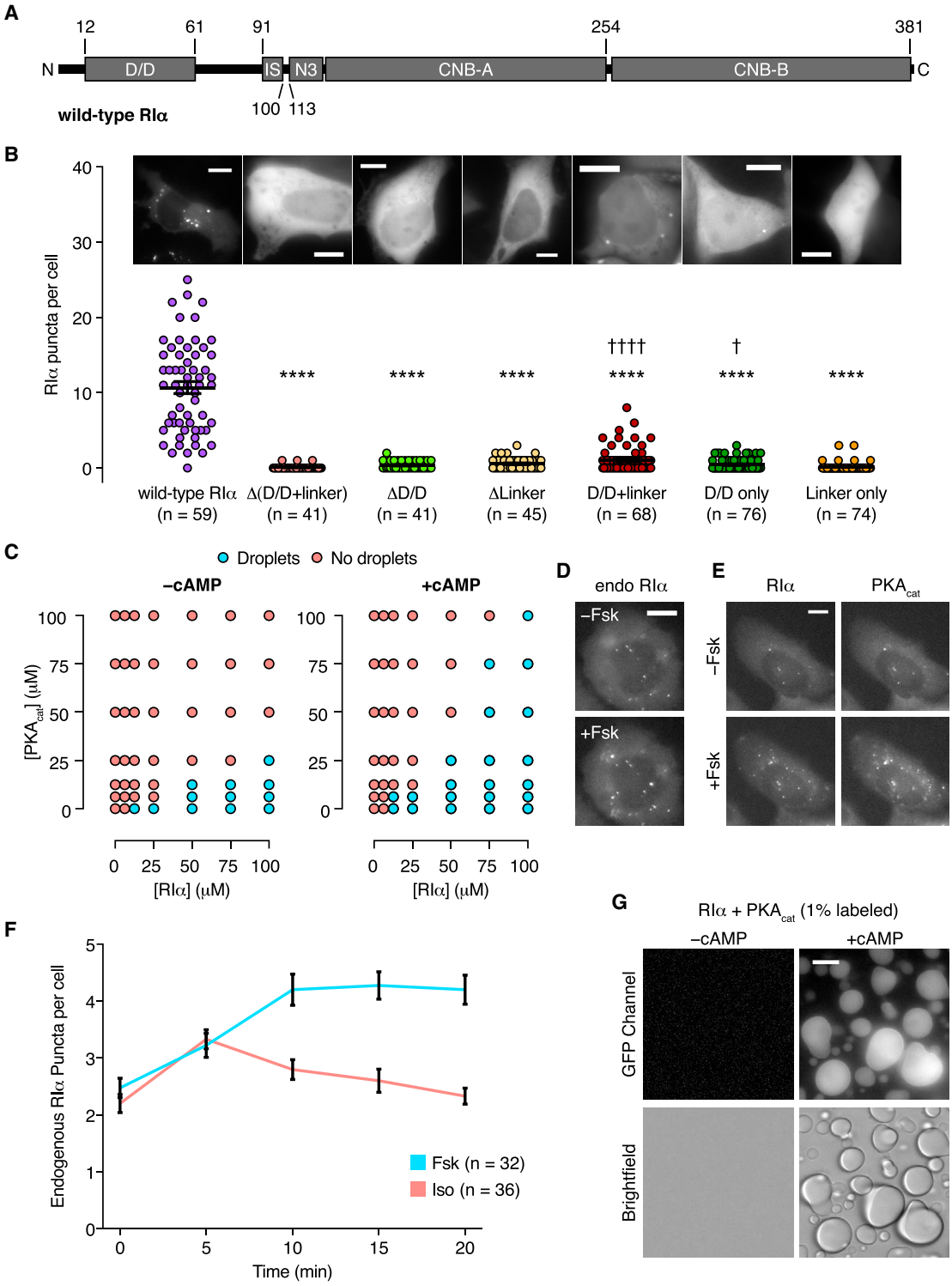

Figure 2. Regulation of RIα Phase Separation by PKA_{cat} and cAMP

(A) Domain structure of full-length, wild-type RIα.

(B) Comparison of RIα punctum number in wild-type HEK293T cells expressing EGFP-tagged wild-type or mutant RIα. The D/D domain (residues 12–61), the linker region (62–113), or both (12–113) were deleted or overexpressed. Horizontal lines indicate mean ± SEM. Representative fluorescence images of HEK293T cells transfected with the corresponding EGFP-tagged RIα constructs are shown above each bar.

(C–G) cAMP enhances RIα phase separation in the presence of PKA_{cat}.

(legend continued on next page)

et al., 2011; Mavrakis et al., 2006). These puncta are highly dynamic, and coalescence of dispersed puncta occurred on the minute scale (Figure 1B; Video S1). Fluorescence recovery after photobleaching (FRAP) experiments indicated that labeled RIα can dynamically exchange between the puncta and diffusible pools, as indicated by similar fluorescence recovery kinetics (time to half maximum [$t_{1/2}$] of 7 s ± 0.44 s, mean ± standard error of the mean [SEM] indicated throughout the paper, n = 12 puncta versus $t_{1/2}$ of 7.8 s ± 0.41 s, n = 5 cytosolic regions) (Figure 1C; Video S2), although labeled RIα showed decreased mobility within puncta ($t_{1/2}$, 35 s ± 1.3 s; n = 9 regions inside RIα puncta; $p < 0.0001$; Figure S1A). In addition, treatment with 2.5% 1,6-hexanediol (Hex), which disrupts weak intermolecular forces present in liquid-like assemblies (Peskett et al., 2018), reduced the number of endogenous RIα puncta per cell by 68% ± 8.6% (Figure 1D).

Strikingly, purified RIα by itself formed liquid droplets *in vitro* (Figure 1E). Increasing molecular crowding with increasing concentrations of polyethylene glycol (PEG) decreased the concentrations of RIα needed for liquid droplet formation (Figure 1F), whereas increasing salt (KCl) concentrations increased the concentrations of RIα needed for liquid droplet formation (Figure S1B). RIα droplets varied in size *in vitro* and in cells (Figure S1C), and although endogenous RIα puncta account for only 0.09% ± 0.02% of the entire cellular volume, we estimated the RIα concentration inside these puncta to be about 5.5 μM (Figures S1D and S1E). We also observed similar fluorescent puncta in various other cell types expressing RIα-GFP, such as cardiomyocytes, astrocytes, and neurons (Figures S1F–S1H). Together, these data indicate that RIα is capable of forming biomolecular condensates and that it does so at endogenous expression levels.

RIα Phase Separation Is Inhibited by PKA_{cat} and Enhanced by cAMP

RIα forms an obligate dimer via its N-terminal dimerization and docking (D/D) domain, which bridges its binding to A-kinase anchoring proteins (AKAPs). Connecting the D/D domain and cAMP binding domains is a linker region that is relatively disordered (STAR Methods) and contains an inhibitory sequence that acts as a pseudosubstrate for PKA_{cat} (Figure 2A; Kim et al., 2005). To probe the role of these domains in RIα LLPS, we generated a panel of EGFP-tagged RIα truncation mutants and monitored their ability to form puncta when overexpressed in wild-type HEK293T cells. No puncta were observed with mutants lacking the D/D domain or the linker region (Figures 2B and S2A–S2E), in contrast to the wild-type control, whereas fluorescent puncta were observed in cells expressing a truncation mutant containing only these two regions (Figure 2B). These data suggest that a segment containing the D/D domain and linker region is necessary and, to some extent, sufficient for RIα LLPS.

The inhibitory sequence and a portion of the linker region become disordered when cAMP-bound RIα is dissociated from PKA_{cat} (Kim et al., 2005). Because this region is involved in RIα LLPS, we hypothesized that PKA_{cat} and cAMP might directly influence this process. Indeed, increasing concentrations of purified PKA_{cat} increased the minimal RIα concentration required for liquid droplet formation *in vitro* (Figure 2C). Moreover, overexpression of PKA_{cat} in $GFP_{1–10}$-expressing 293-RIα cells decreased the number of endogenous RIα puncta per cell by 67% ($p = 0.001$; $-PKA_{cat}$, n = 18 cells; $+PKA_{cat}$, n = 16 cells) in the basal state (Figure S2F).

On the other hand, cAMP directly enhances RIα LLPS in the presence of PKA_{cat} because addition of cAMP attenuated the inhibitory effect of PKA_{cat} on RIα liquid droplet formation *in vitro* and allowed liquid droplet formation at lower RIα concentrations (Figure 2C). In 293-RIα cells expressing $GFP_{1–10}$, stimulation with the AC activator forskolin (Fsk) to elevate cAMP induced an acute increase in endogenous RIα puncta (70% ± 12%, n = 32 cells) (Figures 2D and 2F). Furthermore, increasing cAMP levels through the β-adrenergic receptor agonist isoproterenol transiently increased the number of endogenous RIα puncta per cell (Figure 2F), consistent with the cAMP dynamics induced by this GPCR agonist (DiPilato and Zhang, 2009; Rich et al., 2001). These data suggest that cAMP-bound RIα is more prone to undergo LLPS, consistent with an increase in disorder within the inhibitory sequence and linker region when cAMP-bound RIα dissociates from PKA_{cat}. To observe the localization of PKA_{cat} in this process, we stimulated HEK293T cells overexpressing RIα and PKA_{cat} with Fsk and observed a 164% ± 32% increase in the number of RIα puncta per cell, and PKA_{cat} co-localized with RIα puncta (Figures 2E, S2G, and S2H; Video S3; n = 22 cells). Consistent with this observation, PKA_{cat} (1% GFP-tagged) formed liquid droplets *in vitro* when mixed with RIα and cAMP (Figure 2G) but did not form liquid droplets on its own (Figure S5B). These results suggest that cAMP dynamics dictate formation and dissolution of RIα phase-separated bodies and that PKA_{cat} co-phase-separates with RIα.

RIα Condensates Recruit and Retain High cAMP Levels and PKA Activity

The observed enrichment of PKA_{cat} in RIα phase-separated bodies prompted us to directly probe PKA activity in these

(C) Representative *in vitro* phase diagram of RIα liquid droplet formation as a function of RIα and PKA_{cat} concentration in the presence (right) or absence (left) of 10 μM cAMP. Each condition was assessed at least twice.
(D) Representative fluorescence images of $GFP_{1–10}$-transfected 293-RIα cells before (t = 0, top) and after (t = 10 min, bottom) addition of 50 μM Fsk.
(E) Representative fluorescence images of wild-type HEK293T cells transfected with EGFP-RIα and mTagBFP2-PKA_{cat} before (t = 0, top) and after (t = 10 min, bottom) addition of 50 μM Fsk.
(F) Average time courses of the number of RIα puncta per cell in 293-RIα cells transfected with $GFP_{1–10}$ and treated with 50 μM Fsk (blue curve) or 10 μM isoproterenol (Iso) (red curve). Error bars indicate ± SEM.
(G) Representative GFP (top) and DIC (bottom) images of 50 μM RIα mixed with 25 μM PKA_{cat} (1% GFP-tagged), showing PKA_{cat} in RIα liquid droplets without (left) and with (right) 10 μM cAMP.
Scale bars, 10 μm. †$p = 0.0258$ and ††††$p < 0.0001$ vs Δ(D/D+linker), ****$p < 0.0001$ vs wild-type RIα; Kruskal-Wallis test followed by Dunn's multiple-comparisons test.

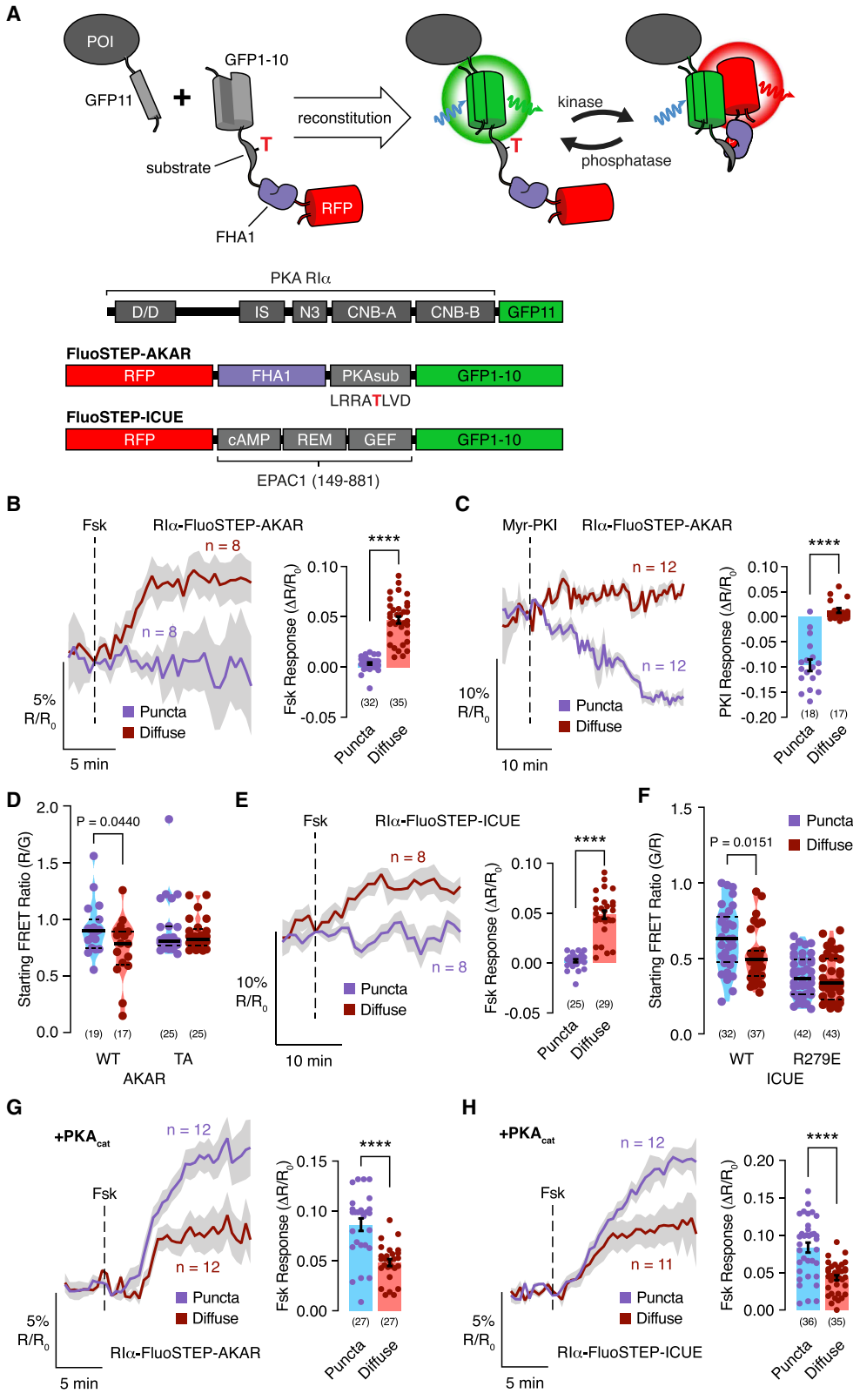

(legend on next page)

bodies. To perform these measurements at the endogenous level, we designed fluorescent sensors targeted to endogenous proteins (FluoSTEPs), a class of fluorescence resonance energy transfer (FRET)-based biosensors that contain sensing domains sandwiched between mRuby2 (acceptor) and $GFP_{1–10}$ (partial donor). The FRET donor fully reconstitutes in the presence of GFP_{11} fused to an endogenous protein of interest, resulting in assembly of functional biosensors only at endogenous protein loci. We designed FluoSTEP-AKAR based on previously established PKA activity-sensing domain consisting of a surrogate PKA substrate sequence (LRRA**T**LVD) and forkhead associated domain 1 (FHA1) as the phosphoamino acid-binding domain (Figure 3A; Zhang et al., 2005). When PKA is active, phosphorylation of the PKA substrate and its subsequent binding to FHA1 are expected to induce a conformational change and an increase in the red/green emission ratio (Figure S3A).

In 293-RIα cells expressing FluoSTEP-AKAR, Fsk induced a 4.7% ± 0.35% increase in the red/green emission ratio (raw emission ratios [R]: $R_{t = 0}$ to $R_{t = end}$, 0.82 to 0.86; n = 35 cells) in diffuse RIα regions (Figure 3B) but no detectable changes within RIα puncta ($R_{t = 0}$ to $R_{t = end}$, 0.88 to 0.86; n = 32 cells), indicating clear differences in PKA activity despite the limited dynamic range of this first-generation technology. Conversely, the cell-permeable, myristoylated Protein Kinase A inhibitor (PKI) induced no detectable ratio changes in diffuse RIα regions ($R_{t = 0}$ to $R_{t = end}$, 0.79 to 0.81; n = 17 cells) under the same conditions but induced a 9.6% ± 1.1% ($R_{t = 0}$ to $R_{t = end}$, 0.89 to 0.81; n = 18 cells) decrease in the red/green emission ratio in RIα puncta (Figure 3C), suggesting that basal PKA activity within RIα phase-separated bodies is high enough to saturate FluoSTEP-AKAR prior to stimulation. Indeed, prior to any stimulation, the initial red/green emission ratio was higher in RIα puncta regions compared with diffuse RIα regions (Figure 3D). As a control, 293-RIα cells transfected with FluoSTEP-AKAR T/A, which contains a threonine-to-alanine (T/A) mutation within the PKA substrate (Zhang et al., 2005), showed no significant red/green ratio difference between RIα puncta and diffuse regions (Figure 3D). The observed high basal emission ratio is consistent with enrichment of PKA activity in RIα phase-separated bodies, although exclusion of phosphatases from RIα condensates could also contribute to the observed effect.

To similarly probe cAMP dynamics within RIα puncta, we utilized a FluoSTEP indicator of cAMP using Epac (ICUE) designed based on the same split biosensor approach (Figure 3A). After reconstitution of the donor fluorophore, cAMP binding to a truncated fragment of Epac1, a previously established cAMP-sensing domain (DiPilato and Zhang, 2009) that includes the cAMP binding domain, Ras exchange motif (REM), and guanine exchange factor (GEF) domain, induces a conformational change and an increase in the green/red emission ratio (Figures S3B and S3C). In 293-RIα cells transfected with FluoSTEP-ICUE, Fsk induced no detectable changes in RIα punctum regions ($R_{t = 0}$ to $R_{t = end}$, 0.61 to 0.61; n = 25 cells) but induced a 4.9% ± 0.4% increase in the green/red emission ratio in diffuse RIα regions ($R_{t = 0}$ to $R_{t = end}$, 0.57 to 0.59; n = 29 cells) (Figure 3E), suggesting that basal cAMP levels in RIα phase-separated bodies are also able to saturate FluoSTEP-ICUE prior to stimulation. As an indication of basal cAMP levels, the initial green/red emission ratio for FluoSTEP-ICUE was higher in RIα punctum regions compared with diffuse RIα regions, whereas introducing an R279E mutation to inhibit cAMP binding (DiPilato et al., 2004) abolished this difference (Figure 3F). Importantly, the dynamic range of our cAMP biosensor was not affected by localization to RIα puncta, as demonstrated by identical green/red emission ratio increases inside and outside of puncta in cells expressing RIα-tethered green/red ICUE and treated with the AC inhibitor MDL-12330A (MDL) followed by a cAMP analog (Figure S3D). Notably, the emission ratio of the punctum-localized sensor gradually decreased to that in diffuse regions after MDL addition (Figure S3D), and a fluorescently labeled cAMP analog (8-Φ-450-cAMP) localized almost exclusively to RIα liquid droplets *in vitro* (Figures S3E–S3G), further supporting high basal cAMP levels within these puncta.

Next, we examined how PKA activity and cAMP dynamics changed during formation of RIα puncta. In PKA_{cat}-expressing 293-RIα cells that showed Fsk-induced punctum formation (Figure S2F), Fsk induced a larger increase in the FluoSTEP-AKAR red/green emission ratio (8.6% ± 0.63%; $R_{t = 0}$ to $R_{t = end}$, 0.8

Figure 3. Endogenous RIα Condensates Form cAMP/PKA Compartments and Enable PDE-Mediated cAMP Compartmentation

(A) Top: fluorescent sensors targeted to endogenous proteins (FluoSTEPs) utilize split-GFP complementation to recruit a biosensor (e.g., FluoSTEP-AKAR) to a protein of interest (POI) expressed at endogenous levels. Bottom: domain structures of RIα-GFP_{11}, FluoSTEP-AKAR, and FluoSTEP-ICUE.

(B–F) Basal PKA activity and cAMP levels within RIα phase-separated bodies are high enough to saturate FluoSTEP responses prior to stimulation.

(B and C) Left: red/green (R/G) emission ratio changes in 293-RIα cells transfected with FluoSTEP-AKAR and stimulated with 50 μM Fsk (B) or 20 μM myristoylated PKI (Myr-PKI) (C). RIα punctum (blue curve) and non-punctum regions (red curve) were analyzed separately. Right: response to Fsk (B) (n = 32 puncta and 35 diffuse regions from 32 cells) or Myr-PKI (C) treatment.

(D) Raw starting emission ratios for FluoSTEP-AKAR and FluoSTEP-AKAR T/A. RIα punctum and non-punctum regions were analyzed separately (wild-type [WT] AKAR, n = 19 puncta and 17 diffuse regions from 17 cells; AKAR T/A, n = 25 puncta and 25 diffuse regions from 25 cells).

(E) Left: green/red (G/R) emission ratio changes in 293-RIα cells transfected with FluoSTEP-ICUE and stimulated with 50 μM Fsk. RIα punctum (blue curve) and non-punctum regions (red curve) were analyzed separately. Right: response to Fsk stimulation.

(F) Raw starting emission ratios for FluoSTEP-ICUE and FluoSTEP-ICUE R279E (WT ICUE, n = 32 puncta and 37 diffuse regions from 32 cells; ICUE R279E, n = 42 puncta and 43 diffuse regions from 42 cells).

(G and H) Left: R/G (G) and G/R (H) emission ratio changes in 293-RIα cells transfected with FluoSTEP-AKAR (G) or FluoSTEP-ICUE (H) plus mTagBFP2-PKA_{cat} and stimulated with 50 μM Fsk. Newly formed RIα punctum regions (blue curve) and non-punctum regions (red curve) were analyzed separately (FluoSTEP-AKAR, n = 12 new puncta and 12 diffuse regions from 12 cells; FluoSTEP-ICUE, n = 11 new puncta and 12 diffuse regions from 11 cells). Right: responses to Fsk stimulation (FluoSTEP-AKAR, n = 27 new puncta and 27 diffuse regions from 27 cells; FluoSTEP-ICUE, n = 35 new puncta and 36 diffuse regions from 35 cells). Solid lines in (B), (C), (E), (G), and (H) indicate representative average time courses of R/G (B, C, and G) and G/R (D and H) emission ratio changes; shaded areas, SEM. Bar graphs in (B), (C), (E), (G), and (H) show maximum emission ratio changes upon drug addition, with bars indicating mean ± SEM. Violin plots in (D) and (F) show the median and quartiles as solid and dashed lines, respectively. ****$p < 0.0001$, unpaired two-tailed Student's t test with Welch's correction.

to 0.87; n = 27 cells) in newly formed RIα puncta compared with the constantly diffuse RIα regions (4.8% ± 0.35%; $R_{t = 0}$ to $R_{t = end}$, 0.8 to 0.82; n = 27 cells) (Figure 3G). Similarly, Fsk-induced Fluo-STEP-ICUE responses were larger in newly formed RIα puncta (8.4% ± 0.66%; $R_{t = 0}$ to $R_{t = end}$, 0.55 to 0.59; n = 35 cells) compared with the constantly diffuse RIα regions (4.3% ± 0.34%; $R_{t = 0}$ to $R_{t = end}$, 0.55 to 0.57; n = 36 cells) (Figure 3H). These results suggest that RIα phase-separated bodies recruit and retain active PKA_{cat} and cAMP.

Dynamic cAMP Buffering by RIα Condensates Drives cAMP Compartmentation

Although cAMP degradation by PDEs has been shown to help create cAMP compartments in cells, PDE activity alone appears to be insufficient to restrict cAMP, given the current understanding of cAMP diffusion characteristics (Boras et al., 2014; Lohse et al., 2017; Yang et al., 2016). Key mechanisms that enable cAMP compartmentation therefore await discovery. Given the high level of cAMP observed in RIα condensates, we hypothesized that these bodies help compartmentalize cAMP by serving as a dynamic buffering system. Using an improved cAMP sensor (ICUE4) (Figures S4A and S4B) fused to the catalytic portion of PDE4D2 ($PDE4D2_{cat}$) ($PDE4D2_{cat}$-ICUE4) (Figures 4A, 4B, and S4C) to monitor local cAMP within PDE compartments (Bock et al., 2020, this issue of *Cell*) as a direct assay for cAMP compartmentation, we found that Fsk induced a small increase in the normalized cyan/yellow emission ratio of only 6.2% ± 0.23% (n = 55 cells), whereas blocking PDE activity by using the PDE4-selective inhibitor rolipram and a general PDE inhibitor, 3-isobutyl-1-methylxanthine (IBMX), rescued the response, suggesting that $PDE4D2_{cat}$ can form a cAMP sink under control conditions when the cAMP compartmentation system is intact (Figure 4B). However, when RIα LLPS was disrupted with 2.5% 1,6-hexanediol pretreatment (Figures 4B and S4D–S4F), Fsk induced much greater cAMP accumulation around PDE4D2, indicated by a larger increase in the normalized cyan/yellow emission ratio (30% ± 0.76%, $p < 0.0001$; n = 50 cells) of the $PDE4D2_{cat}$-ICUE4 probe, suggesting that disrupting RIα condensates leads to decreased cAMP buffering and loss of effective cAMP compartmentation. In cells with no RIα LLPS because RIα is homozygously knocked out, Fsk induced similar changes with and without 1,6-hexanediol pretreatment (Figure 4C), suggesting that the effect on cAMP compartmentation is mediated by RIα. The effect of disrupting RIα condensates was even stronger when RIα was overexpressed. In control cells, Fsk induced no detectable changes in the normalized $PDE4D2_{cat}$-ICUE4 emission ratio (−0.40% ± 0.055%, n = 72 cells), suggesting that RIα overexpression further enhances cAMP compartmentation. In sharp contrast, when RIα LLPS was disrupted by 1,6-hexanediol pretreatment, Fsk stimulation induced a large 65% ± 2.0% (n = 30 cells) increase in the normalized emission ratio (Figure 4D) ($p < 0.0001$). Moreover, RIα LLPS decreased basal cAMP levels around the PDE4D2 compartment because the initial cyan/yellow emission ratios for $PDE4D2_{cat}$-ICUE4 were lower when RIα was present versus when RIα was knocked out (Figure S4G).

To identify the key determinants of RIα-mediated cAMP compartmentation, we expressed mRuby2-tagged $RIα_{D/D+linker}$, which can phase-separate but does not bind cAMP, and mRuby2-tagged $RIα_{ΔD/D+linker}$, which can bind to cAMP but cannot phase-separate, in RIα-null cells and measured cAMP levels around $PDE4D2_{cat}$. In both cases, Fsk treatment induced significant increases in cAMP levels around $PDE4D2_{cat}$ irrespective of 1,6-hexanediol pretreatment, and basal cAMP levels around the PDE4D2 compartment were also elevated; the initial cyan/yellow emission ratios for $PDE4D2_{cat}$-ICUE4 were higher for both mutants compared with wild-type RIα (Figures S4G–S4L). These data suggest that formation of RIα condensates and the ability of RIα to sequester cAMP are required for effective cAMP compartmentalization. Moreover, experiments using dye-labeled cAMP suggest that cAMP is essentially "trapped" in the RIα condensates (Figures S3E, S3F, and 4E). Overall, these results highlight a key mechanism of cAMP compartmentation where RIα condensates enable PDEs to function as local cAMP sinks to drive cAMP signaling specificity.

An Oncogenic PKA Fusion Abolishes RIα Phase Separation

Disruption of RIα phase separation leads to defective cAMP compartmentation, and the aberrant cAMP/PKA signaling caused by altered cAMP compartmentation is linked to various diseases (Caretta and Mucignat-Caretta, 2011; Perera and Nikolaev, 2013; Steinberg and Brunton, 2001). FLC is an atypical liver cancer that primarily affects young adults with no pre-existing liver conditions (Sergi, 2015), making the etiology of this cancer enigmatic. Although the DnaJB1-PKA_{cat} fusion oncogene is detected in nearly all FLC patients, the mechanism by which this fusion protein drives FLC is completely unknown (Honeyman et al., 2014; Kastenhuber et al., 2017). Intriguingly, we observed an almost complete absence of RIα puncta formation in HEK293T cells overexpressing DnaJB1-PKA_{cat} and RIα compared with cells overexpressing wild-type PKA_{cat} and RIα (Figures 5A and 5B), consistent with the inhibitory role of DnaJB1-PKA_{cat} on RIα droplet formation *in vitro* (Figure S5A). A kinase-dead, ATP binding-deficient mutant of DnaJB1-PKA_{cat}, DnaJB1-PKA_{cat}^{K72H}, which does not induce FLC in animal models (Kastenhuber et al., 2017), restored RIα LLPS when co-expressed (Figure 5A and 5B), presumably because of reduced affinity for RIα (Lu et al., 2019). Fsk also failed to induce any significant increases in RIα LLPS when DnaJB1-PKA_{cat} or DnaJB1-PKA_{cat}^{K72H} was co-expressed with RIα, in contrast to wild-type PKA_{cat} (Figures 5C and S5C; Video S4), with little RIα LLPS observed in the case of DnaJB1-PKA_{cat} and many RIα puncta observed in the case of DnaJB1-PKA_{cat}^{K72H}.

N-terminal fusion of the 70 amino-acid consensus sequence from DnaJ chaperones such as DnaJB1 (J-domain) abolishes PKA_{cat} myristoylation (Bastidas et al., 2012) and recruits the Hsp70 chaperone to the fusion protein (Turnham et al., 2019). Therefore, we next tested the effect of PKA_{cat} myristoylation and Hsp70 recruitment by the J-domain on RIα LLPS. Mutating the myristoylation site in wild-type PKA_{cat} (PKA_{cat}^{G1A}) significantly decreased the numbers of RIα puncta under basal and Fsk stimulation conditions (Figure 5D). Intriguingly, adding an N-terminal sequence to restore myristoylation to DnaJB1-PKA_{cat} partially reversed the abolishing effect of DnaJB1-PKA_{cat} on basal RIα LLPS (Figure 5D). Furthermore, disrupting the ability

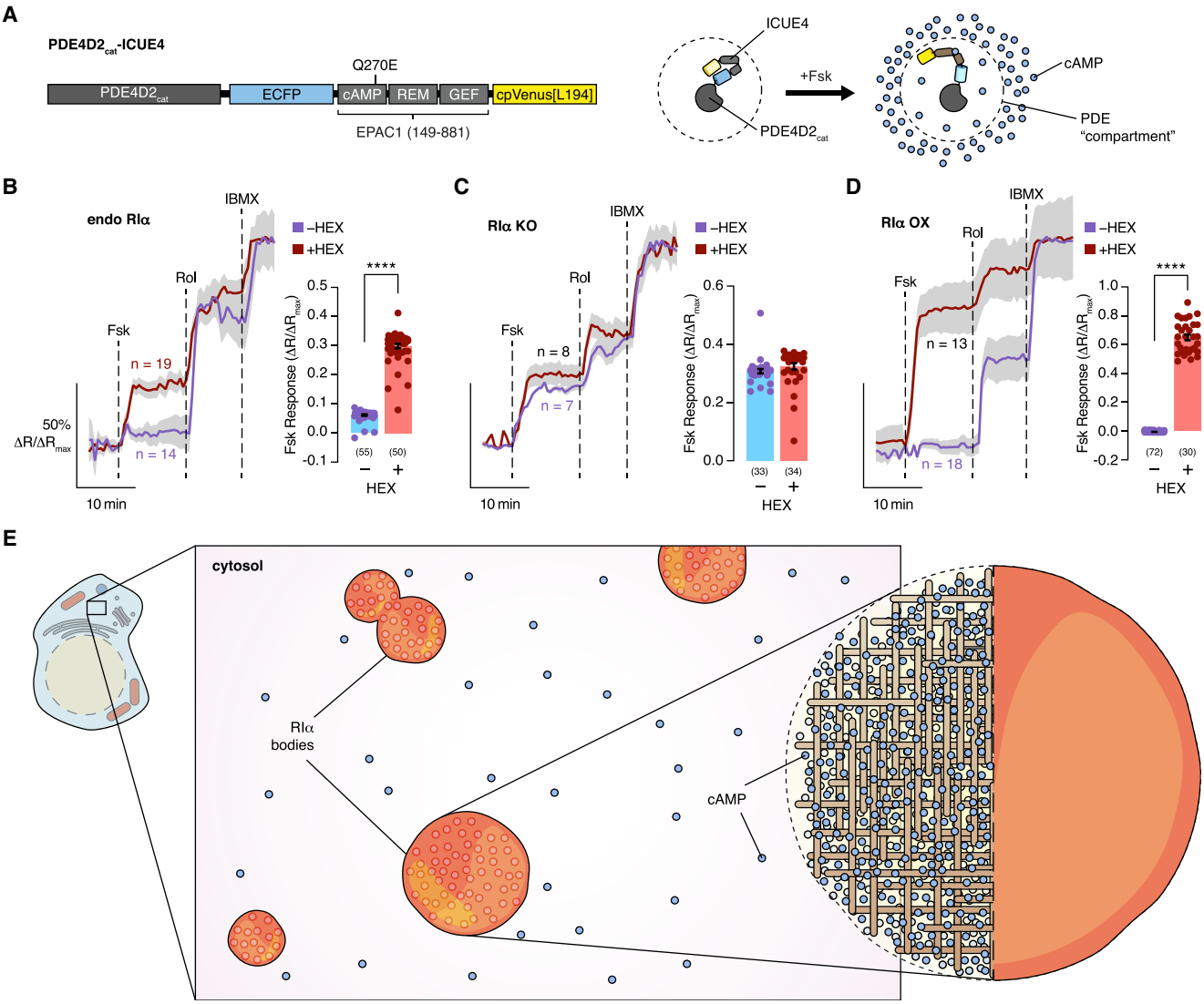

Figure 4. Dynamic cAMP Buffering by RIα Condensates Drives cAMP Compartmentation

(A) Domain structure of the PDE4D2$_{cat}$-ICUE4 sensor, which is used to measure cAMP levels in the PDE4D2 compartment.

(B–D) Investigating the formation of PDE-mediated cAMP sinks with and without RIα phase separation. Left: representative average time courses of cyan/yellow (C/Y) emission ratio changes (normalized to maximum) in WT HEK293T cells transfected with PDE4D2$_{cat}$-ICUE4 (endo RIα) (B), RIα-null HEK293T cells transfected with PDE4D2$_{cat}$-ICUE4 (RIα KO) (C), and HEK293T cells co-transfected with PDE4D2$_{cat}$-ICUE4 and mRuby2-RIα (RIα OX) (D). Cells with (red curve) or without (blue curve) 2.5% Hex pretreatment were stimulated with 50 μM Fsk, 1 μM rolipram (RoI), and 100 μM IBMX. Right: maximum normalized emission ratio upon Fsk stimulation. Solid lines indicate the mean and shaded areas SEM. Bars indicate mean ± SEM.

(E) Schematic illustration of cAMP buffering via RIα phase separation. RIα droplets dynamically sequester cAMP, effectively buffering cAMP in the cytosol. ****$p < 0.0001$, unpaired two-tailed Student's t test with Welch's correction.

of the J-domain to recruit the Hsp70 chaperone by introducing an H33Q mutation (Turnham et al., 2019) in DnaJB1-PKA$_{cat}$ restored cAMP-responsive formation of RIα biomolecular condensates (Figure 5D). Combining these two alterations partially restored basal and Fsk-stimulated punctum formation (Figure 5D). Collectively, these results show that DnaJB1-PKA$_{cat}$ strongly suppresses basal and cAMP-responsive RIα LLPS, which are partly mediated by loss of myristoylation and binding to Hsp70, respectively.

Loss of RIα Phase Separation Disrupts cAMP Compartmentation and Leads to Increased Cell Proliferation and Transformation

Given that RIα LLPS is essential to enable cAMP compartmentation, we expect that DnaJB1-PKA$_{cat}$-induced loss of RIα LLPS should lead to defective cAMP compartmentation. We therefore tested the effect of DnaJB1-PKA$_{cat}$ using our PDE4D2$_{cat}$-ICUE4 cAMP compartmentation assay. In cells expressing wild-type PKA$_{cat}$ and RIα, Fsk induced no detectable changes in the

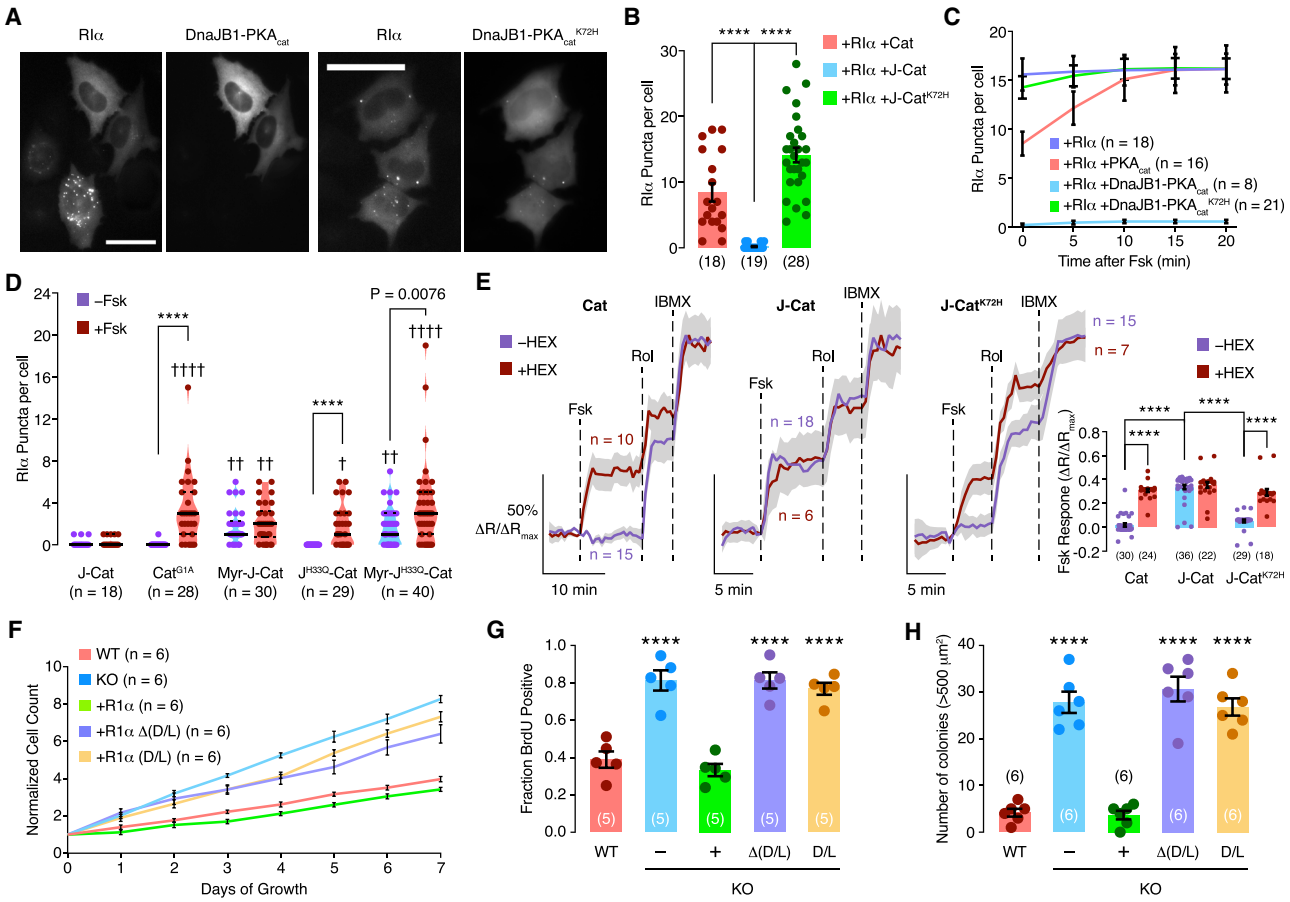

Figure 5. The FLC Oncoprotein DnaJB1-PKA$_{cat}$ Disrupts RIα Phase Separation and cAMP Compartmentation, Resulting in Increased Cell Proliferation and Transformation

(A) Representative fluorescence images of HEK293T cells transfected with EGFP-tagged RIα and mTagBFP2-tagged DnaJB1-PKA$_{cat}$ (left) or DnaJB1-PKA$_{cat}^{K72H}$ (right). Scale bars, 40 μm.

(B) Average number of RIα puncta per cell in HEK293T cells co-transfected with EGFP-RIα and mTagBFP2-tagged PKA$_{cat}$ (Cat), DnaJB1-PKA$_{cat}$ (J-Cat), or DnaJB1-PKA$_{cat}^{K72H}$ (J-Cat^{K72H}). ****p < 0.0001; unpaired two-tailed Student's t test with Welch's correction.

(C) Average time course of the number of RIα puncta per cell following 5 μM Fsk addition to HEK293T cells transfected with EGFP-RIα alone (dark blue curve) or EGFP-RIα plus mTagBFP2-tagged PKA$_{cat}$ (red curve), DnaJB1-PKA$_{cat}$ (light blue curve), or DnaJB1-PKA$_{cat}^{K72H}$ (green curve).

(D) Comparison of RIα punctum number between cells expressing RIα plus DnaJB1-PKA$_{cat}$ (J-Cat), WT PKA$_{cat}$ with no myristoylation (Cat^{G1A}); DnaJB1-PKA$_{cat}$ with the myristoylation consensus sequence at the N terminus (Myr-J-Cat); DnaJB1-PKA$_{cat}$that cannot bind to Hsp70 (J^{H33Q}-Cat); or DnaJB1-PKA$_{cat}$ with myristoylation and no Hsp70 binding (Myr-J^{H33Q}-Cat). Cells were treated with (red) or without (blue) 50 μM Fsk. **** p < 0.0001; Mann-Whitney U test. †p = 0.0198, J^{H33Q}-Cat + Fsk versus J-Cat + Fsk; ††p = 0.0012, Myr-J-Cat – Fsk versus J-Cat – Fsk; ††p = 0.0021, Myr-J-Cat + Fsk versus J-Cat + Fsk; ††p = 0.0039, Myr-J^{H33Q}-Cat – Fsk versus J-Cat – Fsk; ††††p < 0.0001 versus J-Cat + Fsk; Kruskal-Wallis test followed by Dunn's multiple comparisons test.

(E) Representative average time courses of C/Y emission ratio changes (normalized to maximum) in HEK293T cells transfected with PDE4D2$_{cat}$-ICUE4 and mTagBFP2-RIα plus mCherry-tagged PKA$_{cat}$ (Cat), DnaJB1-PKA$_{cat}$ (J-Cat), or DnaJB1-PKA$_{cat}^{K72H}$ (J-Cat^{K72H}). Cells with (red curves) or without (blue curves) 2.5% Hex pretreatment were stimulated with 50 μM Fsk, 1 μM Rol, and 100 μM IBMX. Solid lines indicate the mean and shaded areas SEM. Inset: maximum normalized emission ratio change upon Fsk stimulation for each condition. ****p < 0.0001; unpaired two-tailed Student's t test.

(F–H) Loss of RIα phase separation or cAMP sequestration promotes tumorigenic phenotypes in AML12 hepatocytes. RIα-null cells were transfected with RIα$_{D/D+Linker}$, which permits RIα phase separation but lacks cAMP binding, or RIα$_{Δ(D/D+Linker)}$, which retains cAMP binding but lacks phase separation.

(F) Average time courses of the cell count for AML12 cells under different conditions. Error bars indicate SEM.

(G) Average percentage of bromodeoxyuridine-positive (BrdU+) AML12 cells. ****p < 0.0001 versus WT; ordinary one-way ANOVA followed by Dunnet's multiple comparisons test.

(H) Average number of colonies larger than 500 μm^2 grown in soft agar. ****p < 0.0001 versus WT; ordinary one-way ANOVA followed by Dunnet's multiple comparisons test.

Bars in (B), (E), (G), and (H) indicate mean ± SEM. Violin plots in (D) show the median and quartiles as solid and dashed lines, respectively.

normalized cyan/yellow emission ratio of PDE4D2$_{cat}$-ICUE4 (2.0% ± 1.5%, n = 30 cells) but induced a large (31% ± 1.3%, n = 24 cells) increase in the normalized cyan/yellow emission ratio under these same conditions when RIα LLPS was disrupted by 1,6-hexanediol pretreatment (Figure 5E) (p < 0.0001). On the other hand, cells overexpressing DnaJB1-PKA$_{cat}$ showed

similar Fsk-induced PDE4D2$_{cat}$-ICUE4 responses regardless of 1,6-hexanediol pretreatment (Figure 5E). However, in the presence of DnaJB1-PKA$_{cat}^{K72H}$, which restores RIα LLPS, Fsk again induced only a small increase in the normalized PDE4D2$_{cat}$-ICUE4 emission ratio (5.4% ± 1.2%, n = 29 cells) versus a much larger (29% ± 2.8%, n = 18 cells) increase when RIα LLPS was disrupted by 1,6-hexanediol pretreatment (Figure 5E; $p < 0.0001$). Altogether, these data show that disruption of RIα LLPS by DnaJB1-PKA$_{cat}$ dramatically impairs cAMP compartmentation, providing a mechanistic clue for aberrant signaling caused by this oncoprotein fusion.

A critical question is whether loss of RIα LLPS and subsequent disruption of cAMP compartmentation could have a functional effect on cellular processes, particularly with respect to tumorigenesis. To test the functional consequences of loss of RIα LLPS, we generated an RIα-null cell line by using non-tumorigenic hepatocytic AML12 cells in which we stably expressed wild-type or various mutant forms of RIα and measured their proliferation rates and transformation capabilities. Strikingly, loss of RIα increased cell proliferation and DNA synthesis by 2-fold compared with wild-type cells. In RIα-null cells, re-expressing wild-type RIα rescued the wild-type phenotype, whereas stably expressing RIα mutants that were defective in LLPS or cAMP binding failed to rescue (Figures 5F and 5G; $p < 0.0001$). Moreover, loss of RIα led to formation of detectable colonies on soft agar (Figures 5H and S5D; $p < 0.0001$), suggesting that loss of RIα leads to anchorage-independent growth, a hallmark of cancer cells. Similar to what was observed for cell proliferation, restoration of wild-type RIα in RIα-null cells inhibited colony formation, whereas RIα-null cells expressing RIα mutants that were defective in LLPS or cAMP binding continued to exhibit anchorage-independent growth (Figures 5H and S5D; $p < 0.0001$). These results suggest that loss of RIα LLPS and disrupted cAMP compartmentation lead to tumorigenic phenotypes in hepatocytes. Similar results were also observed with mouse embryonic fibroblasts (Figures S5E–S5G), suggesting that the tumor-suppressive nature of RIα LLPS has broad implications.

DISCUSSION

cAMP compartmentation is crucial for our understanding of how this pathway achieves signaling specificity (Baillie, 2009; Steinberg and Brunton, 2001); however, the mechanisms responsible for compartmentalizing this ubiquitous second messenger are unclear (Lohse et al., 2017; Yang et al., 2016). Local degradation of cAMP has been suggested as a key mechanism in spatially constraining cAMP and forming cAMP compartments (Conti et al., 2014; Stangherlin and Zaccolo, 2012), but the discrepancy between the modest catalytic capabilities of these enzymes (Conti and Beavo, 2007; Goraya et al., 2008) and the reportedly rapid diffusion of cAMP in cells (Bacskai et al., 1993; Chen et al., 1999; Nikolaev et al., 2004) calls into question the dominant role assigned to PDEs (Lohse et al., 2017). In contrast, our companion paper (Bock et al., 2020) estimated a PDE4A1 turnover number of ~160 molecules/s in intact cells, ~30 times faster than *in vitro* estimates (Lohse et al., 2017). They further revealed that cAMP appears to be largely immobile in the basal state, exhibiting buffered diffusion, which results in low free cAMP concentrations and ultimately allows PDEs to create functionally relevant nanodomains of low cAMP concentration. Here we showed that RIα biomolecular condensates act as a dynamic "sponge" in recruiting and retaining cAMP and active PKA$_{cat}$, processes required for cAMP compartmentation, because disrupting these condensates leads to loss of PDE-mediated cAMP sinks. This work thus fills a key gap in our understanding of this fundamental process by uncovering a crucial mechanism to enable cAMP compartmentation. Thermodynamically, RIα phase-separated bodies and the surrounding cytosol can be considered mixtures of cAMP, RIα, and all other components present. Formation of droplets via LLPS and the non-stoichiometric increase in cAMP in these droplets point to differences in chemical potential (Denbigh, 1951; De Groot and Mazur, 2013; Hyman et al., 2014; Kuiken, 1994) underlying the cAMP concentration difference between RIα bodies and the cytosol. This discovery of a critical cAMP compartmentation system mediated by LLPS might ultimately redefine our understanding of how cAMP compartmentation shapes the cAMP/PKA signaling landscape to achieve functional diversity. Future studies will further characterize RIα biomolecular condensates to determine whether other components, such as AKAPs and phosphatases, are present.

Increasing evidence suggests that LLPS acts as a principal organizer of numerous cellular processes, such as actin polymerization (Li et al., 2012), transcription (Boija et al., 2018; Gibson et al., 2019; Sabari et al., 2018), and stress responses (Brangwynne et al., 2009; Jain et al., 2016; Molliex et al., 2015). Emerging studies have shown that many signaling molecules also undergo LLPS (Cai et al., 2019; Su et al., 2016). Although many macromolecules have been shown to undergo LLPS in cells, how LLPS affects their biochemical activities and functions is often unclear. By engineering FluoSTEPs, we can measure enzyme activity and small-molecule dynamics directly in biomolecular condensates without perturbing the expression levels of their individual constituents. Here we targeted FluoSTEPs to endogenous RIα and measured high cAMP levels and PKA activity in RIα bodies. cAMP levels and PKA activity were particularly enriched and retained in newly formed RIα bodies, suggesting that these condensates dynamically buffer cAMP. These live-cell activity measurements were essential for generating our hypothesis, which led us to discover the cellular function of RIα bodies as a key cAMP compartmentation system critical for signaling specificity in the cAMP/PKA pathway. Because FluoSTEPs have the same modular design as all FRET-based sensors (Greenwald et al., 2018; Zhou et al., 2012), their application is expandable to monitor other signaling activities and should aid in further elucidating the organizing principles of cellular activity architectures, including the role of phase-separated enzymatic assemblies in other systems.

FLC is atypical among liver cancers because it is not correlated with age, cirrhosis, or common markers of liver disease (Sergi, 2015). Although the DnaJB1-PKA$_{cat}$ fusion oncoprotein has been reported to be present in the majority of FLC patients (Dinh et al., 2017; Honeyman et al., 2014), the pathological mechanisms of this oncogenic fusion are completely unknown. From a structural and biochemical standpoint, DnaJB1-PKA$_{cat}$ is largely indistinguishable from wild-type PKA$_{cat}$ with respect

to interaction interface and binding affinity for PKA regulatory subunits (Cao et al., 2019; Cheung et al., 2015), cAMP activation (Cao et al., 2019), and catalytic activity (Cao et al., 2019; Honeyman et al., 2014; Riggle et al., 2016). Furthermore, although DnaJB1-PKA$_{cat}$ is expressed at approximately 10-fold higher levels than wild-type PKA$_{cat}$ because of promoter alterations (Riggle et al., 2016), overexpressing wild-type PKA$_{cat}$ does not induce tumor formation in mice (Kastenhuber et al., 2017), suggesting that expression differences alone are not likely to be the determining factor. Our study provides a mechanistic link between DnaJB1-PKA$_{cat}$ and tumorigenesis. DnaJB1-PKA$_{cat}$ abolishes RIα LLPS, disrupting cAMP compartmentation and deregulating cAMP/PKA signaling. Furthermore, loss of RIα LLPS in non-tumorigenic hepatocytes and fibroblasts leads to tumorigenic phenotypes such as increased cell proliferation and anchorage-independent growth. Interestingly, a subset of FLC patients lack the DnaJB1-PKA$_{cat}$ oncogene but exhibit loss of RIα protein expression (Graham et al., 2018), corroborating our model that loss of RIα LLPS is a key driver of FLC. Mechanistically, loss of myristylation and gain of Hsp70 binding (Turnham et al., 2019) by DnaJB1-PKA$_{cat}$ are partially responsible for blocking RIα LLPS, but other mechanisms might also be involved. Intriguingly, DnaJB1-PKA$_{cat}$ and the related fusion oncoprotein ATP1B1-PKA$_{cat}$ have been detected in intraductal oncocytic papillary neoplasms (Singhi et al., 2020); thus, our finding that loss of cAMP compartmentation drives tumorigenic signaling might be applicable to other cancers. Although multiple studies have shown that emergence or enhancement of LLPS is linked to stress conditions or neurological disease states (Jain et al., 2016; Markmiller et al., 2018; Molliex et al., 2015; Peskett et al., 2018; Wegmann et al., 2018), our work provides a distinct example of LLPS being necessary for normal cellular function, with loss of LLPS leading to disease phenotypes, where only a limited number of examples exist (Bouchard et al., 2018).

In summary, we discovered a membraneless organelle that shapes the PKA signaling landscape. Our results represent a conceptual leap forward in understanding how the cAMP/PKA pathway is dynamically organized. Given the universal nature of cAMP/PKA signaling and the ubiquitous expression of RIα (Cadd and McKnight, 1989), our findings have far-reaching physiological implications for various biological systems, such as cardiomyocytes (Buxton and Brunton, 1983; Nikolaev et al., 2006; Scholten et al., 2007; Yin et al., 2008) and neurons (Gorshkov et al., 2017; Park et al., 2014; Shelly et al., 2010), in which the cAMP/PKA pathway plays diverse roles and RIα punctum formation can be observed (Figure S1). Furthermore, we discovered a link between spatially dysregulated cAMP/PKA signaling and cancer. Overall, our findings showcase the intricacies of signaling activity architectures and the importance of biomolecular condensates in their construction.

STAR★METHODS

Detailed methods are provided in the online version of this paper and include the following:

- KEY RESOURCES TABLE
- RESOURCE AVAILABILITY
  - Lead Contact
  - Materials Availability
  - Data and Code Availability
- EXPERIMENTAL MODEL AND SUBJECT DETAILS
  - Cell culture and transfection
  - Generation of stable cell lines
- METHOD DETAILS
  - Plasmid construction
  - Disorder and charge predictions of RIα
  - Cell counting to measure cell proliferation
  - BrdU staining to measure cell proliferation
  - Soft agar colony formation assay to assess cell transformation
  - Protein purification
  - *In vitro* liquid droplet assays
  - Fluorescent protein intensity calibration to measure RIα concentrations
  - Fluorescence recovery after photobleaching
  - Time-lapse epifluorescence imaging
- QUANTIFICATION AND STATISTICAL ANALYSIS
  - FRET biosensor analysis
  - Quantification of cellular puncta
  - Calculations for the apparent diffusivity of cAMP
  - Statistics and reproducibility

SUPPLEMENTAL INFORMATION

Supplemental Information can be found online at https://doi.org/10.1016/j.cell.2020.07.043.

ACKNOWLEDGMENTS

We thank A. Hong, K.L. Guan, and S. Banerjee for guidance with CRISPR; E. Griffis and D. Bindels for confocal microscopy expertise; D.L. Schmitt for help with neuron and glial experiments; C. Brand for help with cardiomyocyte experiments; Y.L. Ma and Q. Ni for insightful discussions; and A. Nguyen and M. Tong for help with cloning. This work was supported by a National Science Foundation predoctoral fellowship DGE-1650112 to J.Z.Z., a Taiwan MOE scholarship to T.-W.L., AFOSR FA9550-18-1-0051 to P.R., NIH R35 GM130389 to S.S.T., and NIH R35 CA197622 and R01 DK073368 to J.Z.

AUTHOR CONTRIBUTIONS

J.Z.Z. and J.Z. conceived the project. J.Z.Z., T.-W.L., and J.Z. designed experiments. S.M. conceived and B.T. developed FluoSTEPs. J.R.Y. developed ICUE4. J.Z.Z., T.-W.L., and J.-F.Z. performed experiments and analyzed the data. L.M.S., M.F., and P.R. developed the model. S.S.T. and J.Z. supervised the project and coordinated experiments. S.M. generated final figures. J.Z.Z., S.M., and J.Z. wrote the manuscript.

DECLARATION OF INTERESTS

The authors declare no competing interests.

Received: November 8, 2019
Revised: March 30, 2020
Accepted: July 30, 2020
Published: August 24, 2020

REFERENCES

Adikusuma, F., Pfitzner, C., and Thomas, P.Q. (2017). Versatile single-step-assembly CRISPR/Cas9 vectors for dual gRNA expression. PLoS ONE *12*, e0187236.

Agarwal, S.R., Clancy, C.E., and Harvey, R.D. (2016). Mechanisms Restricting Diffusion of Intracellular cAMP. Sci. Rep. *6*, 19577.

Bacskai, B.J., Hochner, B., Mahaut-Smith, M., Adams, S.R., Kaang, B.K., Kandel, E.R., and Tsien, R.Y. (1993). Spatially resolved dynamics of cAMP and protein kinase A subunits in Aplysia sensory neurons. Science *260*, 222–226.

Baillie, G.S. (2009). Compartmentalized signalling: spatial regulation of cAMP by the action of compartmentalized phosphodiesterases. FEBS J. *276*, 1790–1799.

Bastidas, A.C., Deal, M.S., Steichen, J.M., Keshwani, M.M., Guo, Y., and Taylor, S.S. (2012). Role of N-terminal myristylation in the structure and regulation of cAMP-dependent protein kinase. J. Mol. Biol. *422*, 215–229.

Bock, A., Annibale, P., Konrad, C., Hannawacker, A., Anton, S., Maiellaro, I., Zabel, U., Sivaramakrishnan, S., Falcke, M., and Lohse, M.J. (2020). Optical mapping of cAMP signaling at the nanometer scale. Cell *182*, this issue, 1519–1530.

Boija, A., Klein, I.A., Sabari, B.R., Dall'Agnese, A., Coffey, E.L., Zamudio, A.V., Li, C.H., Shrinivas, K., Manteiga, J.C., Hannett, N.M., et al. (2018). Transcription Factors Activate Genes through the Phase-Separation Capacity of Their Activation Domains. Cell *175*, 1842–1855.e16.

Boras, B.W., Kornev, A., Taylor, S.S., and McCulloch, A.D. (2014). Using Markov state models to develop a mechanistic understanding of protein kinase A regulatory subunit RIα activation in response to cAMP binding. J. Biol. Chem. *289*, 30040–30051.

Borowicz, S., Van Scoyk, M., Avasarala, S., Karuppusamy Rathinam, M.K., Tauler, J., Bikkavilli, R.K., and Winn, R.A. (2014). The soft agar colony formation assay. J. Vis. Exp., 51998.

Bouchard, J.J., Otero, J.H., Scott, D.C., Szulc, E., Martin, E.W., Sabri, N., Granata, D., Marzahn, M.R., Lindorff-Larsen, K., Salvatella, X., et al. (2018). Cancer Mutations of the Tumor Suppressor SPOP Disrupt the Formation of Active, Phase-Separated Compartments. Mol. Cell *72*, 19–36.e8.

Boularan, C., and Gales, C. (2015). Cardiac cAMP: production, hydrolysis, modulation and detection. Front. Pharmacol. *6*, 203.

Brangwynne, C.P., Eckmann, C.R., Courson, D.S., Rybarska, A., Hoege, C., Gharakhani, J., Jülicher, F., and Hyman, A.A. (2009). Germline P granules are liquid droplets that localize by controlled dissolution/condensation. Science *324*, 1729–1732.

Brunton, L.L., Hayes, J.S., and Mayer, S.E. (1981). Functional compartmentation of cyclic AMP and protein kinase in heart. Adv. Cyclic Nucleotide Res. *14*, 391–397.

Bruystens, J.G.H., Wu, J., Fortezzo, A., Kornev, A.P., Blumenthal, D.K., and Taylor, S.S. (2014). PKA RIα homodimer structure reveals an intermolecular interface with implications for cooperative cAMP binding and Carney complex disease. Structure *22*, 59–69.

Buxton, I.L., and Brunton, L.L. (1983). Compartments of cyclic AMP and protein kinase in mammalian cardiomyocytes. J. Biol. Chem. *258*, 10233–10239.

Cadd, G., and McKnight, G.S. (1989). Distinct patterns of cAMP-dependent protein kinase gene expression in mouse brain. Neuron *3*, 71–79.

Cai, D., Feliciano, D., Dong, P., Flores, E., Gruebele, M., Porat-Shliom, N., Sukenik, S., Liu, Z., and Lippincott-Schwartz, J. (2019). Phase separation of YAP reorganizes genome topology for long-term YAP target gene expression. Nat. Cell Biol. *21*, 1578–1589.

Cao, B., Lu, T.W., Martinez Fiesco, J.A., Tomasini, M., Fan, L., Simon, S.M., Taylor, S.S., and Zhang, P. (2019). Structures of the PKA RIα Holoenzyme with the FLHCC Driver J-PKACα or Wild-Type PKACα. Structure *27*, 816–828.e4.

Caretta, A., and Mucignat-Caretta, C. (2011). Protein kinase a in cancer. Cancers (Basel) *3*, 913–926.

Chen, C., Nakamura, T., and Koutalos, Y. (1999). Cyclic AMP diffusion coefficient in frog olfactory cilia. Biophys. J. *76*, 2861–2867.

Cheung, J., Ginter, C., Cassidy, M., Franklin, M.C., Rudolph, M.J., Robine, N., Darnell, R.B., and Hendrickson, W.A. (2015). Structural insights into mis-regulation of protein kinase A in human tumors. Proc. Natl. Acad. Sci. USA *112*, 1374–1379.

Conti, M., and Beavo, J. (2007). Biochemistry and physiology of cyclic nucleotide phosphodiesterases: essential components in cyclic nucleotide signaling. Annu. Rev. Biochem. *76*, 481–511.

Conti, M., Mika, D., and Richter, W. (2014). Cyclic AMP compartments and signaling specificity: role of cyclic nucleotide phosphodiesterases. J. Gen. Physiol. *143*, 29–38.

Cooper, D.M.F. (2003). Regulation and organization of adenylyl cyclases and cAMP. Biochem. J. *375*, 517–529.

Day, M.E., Gaietta, G.M., Sastri, M., Koller, A., Mackey, M.R., Scott, J.D., Perkins, G.A., Ellisman, M.H., and Taylor, S.S. (2011). Isoform-specific targeting of PKA to multivesicular bodies. J. Cell Biol. *193*, 347–363.

De Groot, S.R., and Mazur, P. (2013). Non-equilibrium thermodynamics (Courier Corporation).

Denbigh, K.G. (1951). The thermodynamics of the steady state (Wiley).

Depry, C., Allen, M.D., and Zhang, J. (2011). Visualization of PKA activity in plasma membrane microdomains. Mol. Biosyst. *7*, 52–58.

Dinh, T.A., Vitucci, E.C.M., Wauthier, E., Graham, R.P., Pitman, W.A., Oikawa, T., Chen, M., Silva, G.O., Greene, K.G., Torbenson, M.S., et al. (2017). Comprehensive analysis of The Cancer Genome Atlas reveals a unique gene and non-coding RNA signature of fibrolamellar carcinoma. Sci. Rep. *7*, 44653.

DiPilato, L.M., and Zhang, J. (2009). The role of membrane microdomains in shaping beta2-adrenergic receptor-mediated cAMP dynamics. Mol. Biosyst. *5*, 832–837.

DiPilato, L.M., Cheng, X., and Zhang, J. (2004). Fluorescent indicators of cAMP and Epac activation reveal differential dynamics of cAMP signaling within discrete subcellular compartments. Proc. Natl. Acad. Sci. USA *101*, 16513–16518.

Dull, T., Zufferey, R., Kelly, M., Mandel, R.J., Nguyen, M., Trono, D., and Naldini, L. (1998). A third-generation lentivirus vector with a conditional packaging system. J. Virol. *72*, 8463–8471.

Gibson, B.A., Doolittle, L.K., Schneider, M.W.G., Jensen, L.E., Gamarra, N., Henry, L., Gerlich, D.W., Redding, S., and Rosen, M.K. (2019). Organization of Chromatin by Intrinsic and Regulated Phase Separation. Cell *179*, 470–484.e21.

Goraya, T.A., Masada, N., Ciruela, A., Willoughby, D., Clynes, M.A., and Cooper, D.M.F. (2008). Kinetic properties of Ca2+/calmodulin-dependent phosphodiesterase isoforms dictate intracellular cAMP dynamics in response to elevation of cytosolic Ca2+. Cell. Signal. *20*, 359–374.

Gorshkov, K., Mehta, S., Ramamurthy, S., Ronnett, G.V., Zhou, F.-Q., and Zhang, J. (2017). AKAP-mediated feedback control of cAMP gradients in developing hippocampal neurons. Nat. Chem. Biol. *13*, 425–431.

Gottesman, M.M., and Fleischmann, R.D. (1986). The role of cAMP in regulating tumour cell growth. Cancer Surv. *5*, 291–308.

Graham, R.P., Lackner, C., Terracciano, L., González-Cantú, Y., Maleszewski, J.J., Greipp, P.T., Simon, S.M., and Torbenson, M.S. (2018). Fibrolamellar carcinoma in the Carney complex: PRKAR1A loss instead of the classic DNAJB1-PRKACA fusion. Hepatology *68*, 1441–1447.

Greenwald, E.C., Mehta, S., and Zhang, J. (2018). Genetically Encoded Fluorescent Biosensors Illuminate the Spatiotemporal Regulation of Signaling Networks. Chem. Rev. *118*, 11707–11794.

Guan, B., Wang, T.-L., and Shih, IeM. (2011). ARID1A, a factor that promotes formation of SWI/SNF-mediated chromatin remodeling, is a tumor suppressor in gynecologic cancers. Cancer Res. *71*, 6718–6727.

Guerrero, F., Ciragan, A., and Iwaï, H. (2015). Tandem SUMO fusion vectors for improving soluble protein expression and purification. Protein Expr. Purif. *116*, 42–49.

Halperin, S.O., Tou, C.J., Wong, E.B., Modavi, C., Schaffer, D.V., and Dueber, J.E. (2018). CRISPR-guided DNA polymerases enable diversification of all nucleotides in a tunable window. Nature *560*, 248–252.

Honeyman, J.N., Simon, E.P., Robine, N., Chiaroni-Clarke, R., Darcy, D.G., Lim, I.I.P., Gleason, C.E., Murphy, J.M., Rosenberg, B.R., Teegan, L., et al. (2014). Detection of a recurrent DNAJB1-PRKACA chimeric transcript in fibrolamellar hepatocellular carcinoma. Science *343*, 1010–1014.

Houslay, M.D. (2010). Underpinning compartmentalised cAMP signalling through targeted cAMP breakdown. Trends Biochem. Sci. *35*, 91–100.

Hyman, A.A., Weber, C.A., and Jülicher, F. (2014). Liquid-liquid phase separation in biology. Annu. Rev. Cell Dev. Biol. *30*, 39–58.

Jain, S., Wheeler, J.R., Walters, R.W., Agrawal, A., Barsic, A., and Parker, R. (2016). ATPase-Modulated Stress Granules Contain a Diverse Proteome and Substructure. Cell *164*, 487–498.

Jhala, U.S., Canettieri, G., Screaton, R.A., Kulkarni, R.N., Krajewski, S., Reed, J., Walker, J., Lin, X., White, M., and Montminy, M. (2003). cAMP promotes pancreatic beta-cell survival via CREB-mediated induction of IRS2. Genes Dev. *17*, 1575–1580.

Kandel, E.R. (2012). The molecular biology of memory: cAMP, PKA, CRE, CREB-1, CREB-2, and CPEB. Mol. Brain *5*, 14.

Kang, M., Day, C.A., Kenworthy, A.K., and DiBenedetto, E. (2012). Simplified equation to extract diffusion coefficients from confocal FRAP data. Traffic *13*, 1589–1600.

Kastenhuber, E.R., Lalazar, G., Houlihan, S.L., Tschaharganeh, D.F., Baslan, T., Chen, C.C., Requena, D., Tian, S., Bosbach, B., Wilkinson, J.E., et al. (2017). *DNAJB1-PRKACA* fusion kinase interacts with β-catenin and the liver regenerative response to drive fibrolamellar hepatocellular carcinoma. Proc. Natl. Acad. Sci. USA *114*, 13076–13084.

Kim, C., Xuong, N.-H., and Taylor, S.S. (2005). Crystal structure of a complex between the catalytic and regulatory (RIalpha) subunits of PKA. Science *307*, 690–696.

Kroeze, W.K., Sheffler, D.J., and Roth, B.L. (2003). G-protein-coupled receptors at a glance. J. Cell Sci. *116*, 4867–4869.

Kuiken, G.D. (1994). Thermodynamics of irreversible processes: applications to diffusion and rheology (Wiley).

Lam, A.J., St-Pierre, F., Gong, Y., Marshall, J.D., Cranfill, P.J., Baird, M.A., McKeown, M.R., Wiedenmann, J., Davidson, M.W., Schnitzer, M.J., et al. (2012). Improving FRET dynamic range with bright green and red fluorescent proteins. Nat. Methods *9*, 1005–1012.

Leonetti, M.D., Sekine, S., Kamiyama, D., Weissman, J.S., and Huang, B. (2016). A scalable strategy for high-throughput GFP tagging of endogenous human proteins. Proc. Natl. Acad. Sci. USA *113*, E3501–E3508.

Li, M., Wang, X., Meintzer, M.K., Laessig, T., Birnbaum, M.J., and Heidenreich, K.A. (2000). Cyclic AMP promotes neuronal survival by phosphorylation of glycogen synthase kinase 3beta. Mol. Cell. Biol. *20*, 9356–9363.

Li, P., Banjade, S., Cheng, H.-C., Kim, S., Chen, B., Guo, L., Llaguno, M., Hollingsworth, J.V., King, D.S., Banani, S.F., et al. (2012). Phase transitions in the assembly of multivalent signalling proteins. Nature *483*, 336–340.

Lim, C.J., Kain, K.H., Tkachenko, E., Goldfinger, L.E., Gutierrez, E., Allen, M.D., Groisman, A., Zhang, J., and Ginsberg, M.H. (2008). Integrin-mediated protein kinase A activation at the leading edge of migrating cells. Mol. Biol. Cell *19*, 4930–4941.

Lohse, C., Bock, A., Maiellaro, I., Hannawacker, A., Schad, L.R., Lohse, M.J., and Bauer, W.R. (2017). Experimental and mathematical analysis of cAMP nanodomains. PLoS ONE *12*, e0174856.

Lu, T.-W., Wu, J., Aoto, P.C., Weng, J.-H., Ahuja, L.G., Sun, N., Cheng, C.Y., Zhang, P., and Taylor, S.S. (2019). Two PKA RIα holoenzyme states define ATP as an isoform-specific orthosteric inhibitor that competes with the allosteric activator, cAMP. Proc. Natl. Acad. Sci. USA *116*, 16347–16356.

Maiellaro, I., Lohse, M.J., Kittel, R.J., and Calebiro, D. (2016). cAMP Signals in Drosophila Motor Neurons Are Confined to Single Synaptic Boutons. Cell Rep. *17*, 1238–1246.

Markmiller, S., Soltanieh, S., Server, K.L., Mak, R., Jin, W., Fang, M.Y., Luo, E.C., Krach, F., Yang, D., Sen, A., et al. (2018). Context-Dependent and Disease-Specific Diversity in Protein Interactions within Stress Granules. Cell *172*, 590–604.e13.

Mavrakis, M., Lippincott-Schwartz, J., Stratakis, C.A., and Bossis, I. (2006). Depletion of type IA regulatory subunit (RIalpha) of protein kinase A (PKA) in mammalian cells and tissues activates mTOR and causes autophagic deficiency. Hum. Mol. Genet. *15*, 2962–2971.

Miyamoto, S., Purcell, N.H., Smith, J.M., Gao, T., Whittaker, R., Huang, K., Castillo, R., Glembotski, C.C., Sussman, M.A., Newton, A.C., and Brown, J.H. (2010). PHLPP-1 negatively regulates Akt activity and survival in the heart. Circ. Res. *107*, 476–484.

Molliex, A., Temirov, J., Lee, J., Coughlin, M., Kanagaraj, A.P., Kim, H.J., Mittag, T., and Taylor, J.P. (2015). Phase separation by low complexity domains promotes stress granule assembly and drives pathological fibrillization. Cell *163*, 123–133.

Nikolaev, V.O., Bünemann, M., Hein, L., Hannawacker, A., and Lohse, M.J. (2004). Novel single chain cAMP sensors for receptor-induced signal propagation. J. Biol. Chem. *279*, 37215–37218.

Nikolaev, V.O., Bünemann, M., Schmitteckert, E., Lohse, M.J., and Engelhardt, S. (2006). Cyclic AMP imaging in adult cardiac myocytes reveals far-reaching β1-adrenergic but locally confined β2-adrenergic receptor-mediated signaling. Circ. Res. *99*, 1084–1091.

Park, A.J., Havekes, R., Choi, J.H., Luczak, V., Nie, T., Huang, T., and Abel, T. (2014). A presynaptic role for PKA in synaptic tagging and memory. Neurobiol. Learn. Mem. *114*, 101–112.

Patra, C., and Brady, M.F. (2018). Biochemistry, cAMP (StatPearls Publishing).

Perera, R.K., and Nikolaev, V.O. (2013). Compartmentation of cAMP signalling in cardiomyocytes in health and disease. Acta Physiol. (Oxf.) *207*, 650–662.

Peskett, T.R., Rau, F., O'Driscoll, J., Patani, R., Lowe, A.R., and Saibil, H.R. (2018). A Liquid to Solid Phase Transition Underlying Pathological Huntingtin Exon1 Aggregation. Mol. Cell *70*, 588–601.e6.

Ran, F.A., Hsu, P.D., Wright, J., Agarwala, V., Scott, D.A., and Zhang, F. (2013). Genome engineering using the CRISPR-Cas9 system. Nat. Protoc. *8*, 2281–2308.

Rich, T.C., Fagan, K.A., Nakata, H., Schaack, J., Cooper, D.M., and Karpen, J.W. (2000). Cyclic nucleotide-gated channels colocalize with adenylyl cyclase in regions of restricted cAMP diffusion. J. Gen. Physiol. *116*, 147–161.

Rich, T.C., Fagan, K.A., Tse, T.E., Schaack, J., Cooper, D.M., and Karpen, J.W. (2001). A uniform extracellular stimulus triggers distinct cAMP signals in different compartments of a simple cell. Proc. Natl. Acad. Sci. USA *98*, 13049–13054.

Richards, M., Lomas, O., Jalink, K., Ford, K.L., Vaughan-Jones, R.D., Lefkimmiatis, K., and Swietach, P. (2016). Intracellular tortuosity underlies slow cAMP diffusion in adult ventricular myocytes. Cardiovasc. Res. *110*, 395–407.

Riggle, K.M., Riehle, K.J., Kenerson, H.L., Turnham, R., Homma, M.K., Kazami, M., Samelson, B., Bauer, R., McKnight, G.S., Scott, J.D., and Yeung, R.S. (2016). Enhanced cAMP-stimulated protein kinase A activity in human fibrolamellar hepatocellular carcinoma. Pediatr. Res. *80*, 110–118.

Sabari, B.R., Dall'Agnese, A., Boija, A., Klein, I.A., Coffey, E.L., Shrinivas, K., Abraham, B.J., Hannett, N.M., Zamudio, A.V., Manteiga, J.C., et al. (2018). Coactivator condensation at super-enhancers links phase separation and gene control. Science *361*, eaar3958.

Saucerman, J.J., Greenwald, E.C., and Polanowska-Grabowska, R. (2014). Mechanisms of cyclic AMP compartmentation revealed by computational models. J. Gen. Physiol. *143*, 39–48.

Scholten, A., van Veen, T.A.B., Vos, M.A., and Heck, A.J.R. (2007). Diversity of cAMP-dependent protein kinase isoforms and their anchoring proteins in mouse ventricular tissue. J. Proteome Res. *6*, 1705–1717.

Sergi, C.M. (2015). Hepatocellular Carcinoma, Fibrolamellar Variant: Diagnostic Pathologic Criteria and Molecular Pathology Update. A Primer. Diagnostics (Basel) *6*, 3.

Shelly, M., Lim, B.K., Cancedda, L., Heilshorn, S.C., Gao, H., and Poo, M.M. (2010). Local and long-range reciprocal regulation of cAMP and cGMP in axon/dendrite formation. Science *327*, 547–552.

Singhi, A.D., Wood, L.D., Parks, E., Torbenson, M.S., Felsenstein, M., Hruban, R.H., Nikiforova, M.N., Wald, A.I., Kaya, C., Nikiforov, Y.E., et al. (2020). Recurrent Rearrangements in PRKACA and PRKACB in Intraductal Oncocytic Papillary Neoplasms of the Pancreas and Bile Duct. Gastroenterology *158*, 573–582.e2.

Stangherlin, A., and Zaccolo, M. (2012). Phosphodiesterases and subcellular compartmentalized cAMP signaling in the cardiovascular system. Hear. Circ. Physiol. *302*, H387–H390.

Steinberg, S.F., and Brunton, L.L. (2001). Compartmentation of G protein-coupled signaling pathways in cardiac myocytes. Annu. Rev. Pharmacol. Toxicol. *41*, 751–773.

Su, X., Ditlev, J.A., Hui, E., Xing, W., Banjade, S., Okrut, J., King, D.S., Taunton, J., Rosen, M.K., and Vale, R.D. (2016). Phase separation of signaling molecules promotes T cell receptor signal transduction. Science *352*, 595–599.

Subach, O.M., Cranfill, P.J., Davidson, M.W., and Verkhusha, V.V. (2011). An enhanced monomeric blue fluorescent protein with the high chemical stability of the chromophore. PLoS ONE *6*, e28674.

Terrin, A., Monterisi, S., Stangherlin, A., Zoccarato, A., Koschinski, A., Surdo, N.C., Mongillo, M., Sawa, A., Jordanides, N.E., Mountford, J.C., and Zaccolo, M. (2012). PKA and PDE4D3 anchoring to AKAP9 provides distinct regulation of cAMP signals at the centrosome. J. Cell Biol. *198*, 607–621.

Tillo, S.E., Xiong, W.-H., Takahashi, M., Miao, S., Andrade, A.L., Fortin, D.A., Yang, G., Qin, M., Smoody, B.F., Stork, P.J.S., and Zhong, H. (2017). Liberated PKA Catalytic Subunits Associate with the Membrane via Myristoylation to Preferentially Phosphorylate Membrane Substrates. Cell Rep. *19*, 617–629.

Turnham, R.E., Smith, F.D., Kenerson, H.L., Omar, M.H., Golkowski, M., Garcia, I., Bauer, R., Lau, H.T., Sullivan, K.M., Langeberg, L.K., et al. (2019). An acquired scaffolding function of the DNAJ-PKAc fusion contributes to oncogenic signaling in fibrolamellar carcinoma. eLife *8*, 1–27.

Udenwobele, D.I., Su, R.-C., Good, S.V., Ball, T.B., Varma Shrivastav, S., and Shrivastav, A. (2017). Myristoylation: An Important Protein Modification in the Immune Response. Front. Immunol. *8*, 751.

Wegmann, S., Eftekharzadeh, B., Tepper, K., Zoltowska, K.M., Bennett, R.E., Dujardin, S., Laskowski, P.R., MacKenzie, D., Kamath, T., Commins, C., et al. (2018). Tau protein liquid-liquid phase separation can initiate tau aggregation. EMBO J. *37*, 1–21.

Willoughby, D., and Cooper, D.M.F. (2007). Organization and Ca2+ regulation of adenylyl cyclases in cAMP microdomains. Physiol. Rev. *87*, 965–1010.

Yang, P.C., Boras, B.W., Jeng, M.T., Docken, S.S., Lewis, T.J., McCulloch, A.D., Harvey, R.D., and Clancy, C.E. (2016). A Computational Modeling and Simulation Approach to Investigate Mechanisms of Subcellular cAMP Compartmentation. PLoS Comput. Biol. *12*, e1005005.

Yin, Z., Jones, G.N., Towns, W.H., 2nd, Zhang, X., Abel, E.D., Binkley, P.F., Jarjoura, D., and Kirschner, L.S. (2008). Heart-specific ablation of Prkar1a causes failure of heart development and myxomagenesis. Circulation *117*, 1414–1422.

Zaccolo, M. (2006). Phosphodiesterases and compartmentalized cAMP signalling in the heart. Eur. J. Cell Biol. *85*, 693–697.

Zaccolo, M., and Pozzan, T. (2002). Discrete microdomains with high concentration of cAMP in stimulated rat neonatal cardiac myocytes. Science *295*, 1711–1715.

Zhang, J., Hupfeld, C.J., Taylor, S.S., Olefsky, J.M., and Tsien, R.Y. (2005). Insulin disrupts beta-adrenergic signalling to protein kinase A in adipocytes. Nature *437*, 569–573.

Zhou, X., Herbst-Robinson, K.J., and Zhang, J. (2012). Visualizing dynamic activities of signaling enzymes using genetically encodable FRET-based biosensors from designs to applications. Methods Enzymol. *504*, 317–340.

STAR★METHODS

KEY RESOURCES TABLE

REAGENT or RESOURCE	SOURCE	IDENTIFIER
Bacterial and Virus Strains		
DH5α competent bacteria	NEB	Cat#C2987I
RIα-EGFP lentivirus	This paper	N/A
$RI\alpha_{D/D+Linker}$-EGFP lentivirus	This paper	N/A
$RI\alpha_{\Delta(D/D+Linker)}$-EGFP lentivirus	This paper	N/A
BL21(DE3) competent bacteria	Agilent	Cat#200131
Rosetta (DE3) pLysS competent bacteria	Millipore Sigma	Cat#70956
Biological Samples		
Sprague-Dawley rat pups	Charles River	Strain Code 400
Chemicals, Peptides, and Recombinant Proteins		
BbsI	NEB	Cat#R3539
Q5 High Fidelity Polymerase	NEB	Cat#M0491S
HiFi DNA Assembly Kit	NEB	Cat#E5520S
HindIII	NEB	Cat#R0104S
EcoRI	NEB	Cat#R0101S
XbaI	NEB	Cat#R0145S
Q5 Site Directed Mutagenesis Kit	NEB	Cat#E0554
DMEM:F12	ThermoFisher	Cat#12634010
ITS Liquid Media Supplement	Sigma Aldrich	Cat#I3146
Dexamethasone	Sigma Aldrich	Cat#D1159
Polyjet	Signagen	Cat#SL100688
DNase I	ThermoFisher	Cat#EN0525
Neurobasal media	ThermoFisher	Cat#21103049
SM1 Supplement	STEMCELL Technologies	Cat#05711
Poly-D-Lysine	Sigma Aldrich	Cat#P6407
Lipofectamine LTX	Invitrogen	Cat#15338500
Puromycin	Sigma Aldrich	Cat#P8833
BSA	Roche	Cat#10738328103
HEPES	Sigma Aldrich	Cat#H3375
EDTA	Sigma Aldrich	Cat#E6758
DAPI	ThermoFisher	Cat#D21490
Noble Agar	ThermoFisher	Cat#AAJ1090722
Powdered DMEM	ThermoFisher	Cat#12800017
IPTG	Sigma Aldrich	Cat#I6758
MES	Sigma Aldrich	Cat#M3671
EGTA	Sigma Aldrich	Cat#E3889
DTT	Sigma Aldrich	Cat#D0632
Protease inhibitors	Roche	Cat#11873580001
cGMP	Sigma Aldrich	Cat#G7504
β-mercaptoethanol	Sigma Aldrich	Cat#M6250
Imidazole	Sigma Aldrich	Cat#1336500
ATP	Sigma Aldrich	Cat#A26209
cAMP	Sigma Aldrich	Cat#A9501
PEG4000	Sigma Aldrich	Cat#1546569

(*Continued on next page*)

Continued

REAGENT or RESOURCE	SOURCE	IDENTIFIER
Forskolin	CalBioChem	Cat#344281
IBMX	Sigma Aldrich	Cat#I7018
Rolipram	Alexis	Cat#61413-54-5
1,6-hexanediol	Sigma Aldrich	Cat#240117
Myr-PKI	Tocris	Cat#2546
Isoproterenol	Sigma Aldrich	Cat#1351005
MDL-12330A	Sigma Aldrich	Cat#B23151
8-Br-2′-O-Me-cAMP-AM	Biolog	Cat#B028-01
8-[Φ-450]-cAMP	Biolog	Cat#P024-001
Critical Commercial Assays		
BrdU kit	Invitrogen	Cat#B23151
Deposited Data		
FluoSTEP-ICUE sequence	GenBank	MT800777.1
FluoSTEP-AKAR sequence	GenBank	MT800778.1
Experimental Models: Cell Lines		
HEK293T	ATCC	ATTC Cat#CRL-11268
HEK293A	ThermoFisher	Cat#R70507
MEF	GS McKnight Lab, University of Washington, Seattle, WA, USA	N/A
AML12	ATCC	ATCC Cat#CRL-2254
293-RIα	This paper	N/A
293T-RIα KO	This paper	N/A
MEF-RIα KO	Day et al., 2011	N/A
AML12-RIα KO	This paper	N/A
AML12-RIα KO-RIα-EGFP	This paper	N/A
AML12-RIα $KO_{D/D+Linker}$-RIα-EGFP	This paper	N/A
AML12-RIα $KO_{\Delta(D/D+Linker)}$-RIα-EGFP	This paper	N/A
MEF-RIα KO-RIα-EGFP	This paper	N/A
MEF-RIα KO-$RIα_{D/D+Linker}$-EGFP	This paper	N/A
MEF-RIα KO-$RIα_{\Delta(D/D+Linker)}$-EGFP	This paper	N/A
Oligonucleotides		
Primers for plasmid construction, see Table S1	This paper	N/A
RIα-FP_{11} HDR ssDNA, see Table S1	IDT, for this paper	N/A
DnaJB1 exon 1 gBlock, see Table S1	IDT, for this paper	N/A
Recombinant DNA		
px458	Ran et al., 2013	Addgene plasmid #48138
px459	Ran et al., 2013	Addgene plasmid #62988
px458 mouse RIα gRNA	This paper	N/A
px459 human RIα gRNA	This paper	N/A
pcDNA3 AKAR2-CR	Lam et al., 2012	Addgene plasmid #40255
pBAD-mTagBFP2	Subach et al., 2011	Addgene plasmid #34632
pcDNA3.1 EGFP-RIα	Day et al., 2011	N/A
pcDNA3.1 mCherry-PKA_{cat}	Day et al., 2011	N/A
pcDNA3.1 mRuby2-RIα	This paper	N/A
pcDNA3.1 mTagBFP2-RIα	This paper	N/A
pcDNA3.1 $RIα_{D/D+Linker}$-EGFP	This paper	N/A
pcDNA3.1 $RIα_{D/D}$-EGFP	This paper	N/A

(*Continued on next page*)

Continued

REAGENT or RESOURCE	SOURCE	IDENTIFIER
pcDNA3.1 RIα$_{Linker}$-EGFP	This paper	N/A
pcDNA3.1 RIα$_{\Delta(D/D+Linker)}$-EGFP	This paper	N/A
pcDNA3.1 RIα$_{\Delta D/D}$-EGFP	This paper	N/A
pcDNA3.1 RIα$_{\Delta Linker}$-EGFP	This paper	N/A
pcDNA3.1 mTagBFP2-PKA$_{cat}$	This paper	N/A
pcDNA3.1 GFP$_{1-10}$	Leonetti et al., 2016	Addgene plasmid #70219
pcDNA3 AKAR4	Depry et al., 2011	Addgene plasmid #61619
pcDNA3 ICUE3	DiPilato and Zhang, 2009	Addgene plasmid #61622
pcDNA3.1 FluoSTEP-AKAR	This paper	N/A
pcDNA3.1 FluoSTEP-ICUE	This paper	N/A
pcDNA3.1 FluoSTEP-AKAR(T/A)	This paper	N/A
pcDNA3.1 FluoSTEP-ICUE(R279E)	This paper	N/A
pcDNA3.1 ICUE4	This paper	N/A
PDE4D2 cDNA	gift from Hengming Ke, UNC, Chapel Hill, NC	N/A
pcDNA3.1 PDE4D2$_{cat}$-ICUE4	This paper	N/A
pcDNA3.1 RIα-ICUE4	This paper	N/A
pcDNA3.1 RIα$_{D/D+Linker}$-ICUE4	This paper	N/A
pcDNA3.1 RG-ICUE	This paper	N/A
pcDNA3.1 RIα-RG-ICUE	This paper	N/A
pcDNA3.1 mCherry-DnaJB1-PKA$_{cat}$	This paper	N/A
pcDNA3.1 mCherry-DnaJB1-PKA$_{cat}^{K72H}$	This paper	N/A
pcDNA3.1 mTagBFP2-DnaJB1-PKA$_{cat}$	This paper	N/A
pcDNA3.1 mTagBFP2-DnaJB1-PKA$_{cat}^{K72H}$	This paper	N/A
pcDNA3.1 mCherry-PKA$_{cat}^{G1A}$	This paper	N/A
pcDNA3.1 mCherry-Myr-DnaJB1-PKA$_{cat}$	This paper	N/A
pcDNA3.1 mCherry-DnaJB1-PKA$_{cat}$	This paper	N/A
pcDNA3.1 mCherry-DnaJB1^{H33Q}-PKA$_{cat}$	This paper	N/A
pcDNA3.1 mCherry-Myr-DnaJB1^{H33Q}-PKA$_{cat}$	This paper	N/A
pLenti-puro	Guan et al., 2011	Addgene plasmid #39481
pLenti RIα-EGFP	This paper	N/A
pLenti RIα$_{D/D+Linker}$-EGFP	This paper	N/A
pLenti RIα$_{\Delta(D/D+Linker)}$-EGFP	This paper	N/A
pRSET B sfGFP	This paper	N/A
pRSET B	Invitrogen	Cat#V35120
pEvolvR-enCas9-PolI3M-TBD	Halperin et al., 2018	Addgene plasmid #113077
pMD2.G	Dull et al., 1998	Addgene plasmid #12259
psPAX2	Dull et al., 1998	Addgene plasmid #12260
pET-His6-SUMO-TEV-LIC-PKA$_{cat}$	Lu et al., 2019	N/A
pET-His6-SUMO-TEV-LIC-DnaJB1-PKA$_{cat}$	Lu et al., 2019	N/A
pET-His6-EGFP-PKA$_{cat}$	Lu et al., 2019	N/A
Software and Algorithms		
MATLAB	MathWorks	https://www.mathworks.com/products/matlab.html
PRISM	Graphpad	https://www.graphpad.com/scientific-software/prism/
Adobe Illustrator	Adobe	https://www.adobe.com/products/illustrator.html
ImageJ	NIH	https://imagej.nih.gov

RESOURCE AVAILABILITY

Lead Contact

Further information and requests for resources and reagents should be directed to and will be fulfilled by the Lead Contact, Jin Zhang (jzhang32@ucsd.edu).

Materials Availability

Plasmids generated in this study will be made available through Addgene and can be shared upon request.

Data and Code Availability

The sequences for FluoSTEP-ICUE and FluoSTEP-AKAR have been uploaded onto GenBank (FluoSTEP-ICUE: MT800777.1; FluoSTEP-AKAR: MT800778.1).

EXPERIMENTAL MODEL AND SUBJECT DETAILS

Cell culture and transfection

HEK293A, HEK293T, and MEF cells were cultured in Dulbecco's modified Eagle medium (DMEM, GIBCO) containing 1 g L^{-1} glucose and supplemented with 10% (v/v) fetal bovine serum (FBS, Sigma) and 1% (v/v) penicillin–streptomycin (Pen-Strep, Sigma-Aldrich). AML12 cells were cultured in DMEM:F12 medium (Thermo Fisher) containing 10% FBS, 10 μg mL^{-1} insulin, 5.5 μg mL^{-1} transferrin, 5 ng mL^{-1} selenium (ITS liquid media supplement, Sigma-Aldrich), and 40 ng mL^{-1} dexamethasone (Sigma-Aldrich). All cells were maintained in a 37°C incubator with a humidified 5% CO_2 atmosphere. Before transfection, HEK293A and HEK293T cells were plated onto sterile poly-D-lysine coated 35-mm glass-bottomed dishes and grown to 50%–70% confluence. HEK293A and HEK293T cells were then transfected using Polyjet (Signagen) and grown for an additional 16-24 h before imaging.

Neonatal rat ventricular myocytes were isolated from cardiac ventricles of 1- to 2-day-old male and female Sprague-Dawley rat pups (Charles River) as described previously (Miyamoto et al., 2010). Neonatal myocytes were plated at a density of 3.0×10^4 cm^{-2} on laminin-coated 35-mm glass-bottomed dishes and maintained in DMEM with 15% FBS overnight. Cells were transfected 24 h later using Polyjet for 48 h, with the media changed 24 h after transfection. Primary rat hippocampal neurons and glial cells were harvested from male and female E19 Sprague-Dawley rat pups (Charles River) in ice-cold Hank's Balanced Salt Solution (HBSS, GIBCO) and were dissociated using the Papain Dissociation System with $MgSO_4$ and DNase I according to the manufacturer's instructions. Dissociated neurons and glial cells were diluted to 200,000 cells mL^{-1} and resuspended in Neurobasal medium (Thermo Fisher) with 2% SM1 supplement (STEMCELL Technologies). Cells were plated onto 35-mm glass-bottom dishes coated with 100 μg mL^{-1} poly-D-lysine (Sigma) and cultured in a 37°C incubator with a humidified 5% CO_2 atmosphere. At 1 or 3 days *in vitro*, cells were transfected with Lipofectamine LTX (Invitrogen) according to the manufacturer's instructions in Neurobasal media and imaged after 48 h. All animals were treated in accordance with the UC San Diego Animal Care and Use Committee guidelines.

Generation of stable cell lines

To generate 293-RIα cells, HEK293A cells were plated in 6-well plates. After 24 h, 1 μg of px459 plasmid (Ran et al., 2013) (gift of Feng Zhang, Addgene plasmid #62988) (encoding Cas9, gRNA, and puromycin resistence gene) and 20 pmol of ssDNA ultramer HDR template (Integrated DNA Technologies; Table S1) were transfected using Polyjet following the manufacturer's protocol. Cells were passaged 1 day after transfection into a 60-mm dish, and 1 μg mL^{-1} puromycin was added 24 h later. When no viable cells remained in the untransfected dish (around 2-3 days), the media was replenished without puromycin. Cells were passaged 24 h later and resuspended in sorting buffer (1 x DPBS with 0.5% BSA, 25 mM HEPES, 1 mM EDTA, pH 7, 2.5 μg mL^{-1} of DNase I (Thermo Fisher)) with 0.1 μg mL^{-1} DAPI (Thermo Fisher). Cells were sorted for DAPI-negative staining and plated as single cells in a 96-well plate using a BD FACS Aria II Cell Sorter. After 3 weeks of incubation, wells containing single-cell colonies were passaged, and DNA was extracted for genotyping using the DNeasy Blood & Tissue Kit (QIAGEN). Genomic PCR was performed using the Q5 High-Fidelity Kit (New England Biolabs) and with primers listed in Table S1. To evaluate the copy number of correct gene edits, PCR products were gel extracted using PureLink Quick Gel Extraction kit (Invitrogen), cloned into TOPO PCR vectors (Invitrogen), and subjected to Sanger sequencing (Genscript).

RIα null HEK293T cells were generated similarly to methods previously described (Ran et al., 2013), but with slight modifications. When cells reached 70% confluency, cells were co-transfected with two px458 plasmids (Ran et al., 2013) (gift of Feng Zhang, Addgene plasmid #48138) (Cas9, gRNA, and GFP) that target RIα. After 24 h of transfection, the cells were aspirated, washed with DPBS, and filtered through a 35-μm cell strainer. Cells with GFP signals were sorted into single cells in a 96-well plate using a BD FACSJazz™ cell sorter. After single cells had grown into colonies, the cells were transferred to 60-mm cell culture plates. The corresponding genomic DNA segment was PCR-amplified using primers listed in Table S1 to verify correct gene editing. Each colony was validated via western blotting and DNA sequencing.

RIα null MEF cells were generated previously (Day et al., 2011). RIα null AML12 (ATCC) cells were generated similarly to RIα knockout HEK293T cells, except the gRNAs differ, and the corresponding genomic DNA segment to verify correct gene editing was PCR amplified using primers listed in Table S1. To generate stable RIα null MEF and AML12 cells with exogenously expressed RIα

mutants, lentiviruses were made by transfection of pLenti backbone versions of RIα mutants with the packaging vectors pMD2.G (gift of Didier Trono, Addgene plasmid #12259) and psPAX2 (gift of Didier Trono, Addgene plasmid #12260) (Dull et al., 1998) into HEK293T cells. At 24 h after transfection, HEK293T cells were replenished with fresh media. After an additional 2 days, supernatant was collected and sterile-filtered through a 0.45 μm filter. RIα null MEF and AML12 cells were infected with lentiviruses and underwent FACS.

METHOD DETAILS

Plasmid construction

RIα CRISPR constructs

All plasmids are in the pcDNA3.1 backbone unless specified and all primers used to generate plasmids are listed in Table S1. All constructs were verified by Sanger sequencing (Genscript). The vector expressing both gRNA and Cas9 in the px459 v2.0 backbone (px459) (Ran et al., 2013) was generated using Golden Gate cloning as previously described (Adikusuma et al., 2017). To construct gRNA expression vectors for generation of the 293-RIα cell line, the 20-bp target sequence was sub-cloned into px459. To generate RIα null HEK293T cells, two designed guide sequences that specifically target the human RIα gene were each cloned into the sgRNA scaffold in px458 (Ran et al., 2013). For RIα null AML12 cells and MEFs, two designed guide sequences that specifically target the mouse RIα gene were each cloned into the sgRNA scaffold in px458.

Fluorescent protein-tagged RIα constructs

EGFP-RIα and mCherry-PKA$_{cat}$ were generated previously (Day et al., 2011). mRuby2-RIα was generated via PCR amplification of mRuby2 from pcDNA3-AKAR2-CR (Lam et al., 2012) (gift of Michael Lin, Addgene plasmid #40255) and RIα from the RIα-EGFP plasmid backbone, followed by Gibson assembly using the NEBuilder Hi-Fi DNA Assembly Cloning Kit (New England Biolabs). mTagBFP2-RIα was generated by Gibson assembly of PCR products amplified from pBAD-mTagBFP2 (Subach et al., 2011) (gift of Vladislav Verkusha, Addgene plasmid #34632). RIα mutants C-terminally tagged with either EGFP or mRuby2 were generated via Gibson assembly of PCR products amplified from RIα-EGFP or RIα-mRuby2. mTagBFP2-PKA$_{cat}$ was constructed by Gibson assembly of PCR products amplified from pBAD-mTagBFP2 (Subach et al., 2011).

FluoSTEP sensor constructs

pcDNA3.1-GFP$_{1-10}$ (Leonetti et al., 2016) was a gift from Bo Huang (Addgene plasmid #70219). To construct FluoSTEP-AKAR, mRuby2 was PCR-amplified from AKAR2-CR (Lam et al., 2012) and the FHA1 and PKA substrate were PCR-amplified from AKAR4 (Depry et al., 2011) (Addgene plasmid #61619). The resulting PCR fragments were Gibson assembled into HindIII- and EcoRI-digested pcDNA3.1 GFP$_{1-10}$. FluoSTEP-ICUE was constructed similarly, except that Epac1$^{149-881}$ was PCR-amplified from ICUE3 (DiPilato and Zhang, 2009) (Addgene plasmid #61622). FluoSTEP-AKAR (T/A) was constructed by Gibson assembly of PCR products amplified from FluoSTEP-AKAR. FluoSTEP-ICUE R279E was constructed by Gibson assembly of PCR products amplified from FluoSTEP-ICUE.

ICUE4 and related constructs

To construct ICUE4, the Q270E point mutation was introduced using site-directed mutagenesis of ICUE3 (DiPilato and Zhang, 2009). To construct PDE4D2$_{cat}$-ICUE4, PDE4D2$^{86-418}$ was PCR-amplified from PDE4D2 cDNA (gift from Hengming Ke, UNC, Chapel Hill, NC), and the ICUE4 backbone was PCR-amplified. The resulting PCR fragments were Gibson assembled. RIα-ICUE4 was constructed by Gibson assembly of PCR products amplified from RIα-EGFP and ICUE4. RIα$_{D/D+Linker}$-ICUE4 was constructed similarly to RIα-ICUE4 using PCR products amplified from RIα$_{D/D+Linker}$-EGFP.

Red-green ICUE sensor constructs

To construct red-green ICUE (RG-ICUE), mRuby2 was PCR-amplified from AKAR2-CR (Lam et al., 2012), superfolder GFP (sfGFP) was PCR-amplified from pcDNA3.1 GFP$_{1-10}$, and Epac1$^{149-881}$ was PCR-amplified from ICUE3 (DiPilato and Zhang, 2009). The resulting PCR fragments were Gibson assembled. To tag RIα with the RG-ICUE sensor, RIα was PCR-amplified from RIα-EGFP construct and RG-ICUE was PCR-amplified. The resulting PCR fragments were Gibson assembled.

PKA$_{cat}$ mutant constructs

mCherry-DnaJB1-PKA$_{cat}$ was generated using DNA gBlock segments (Table S1) designed and synthesized with connecting sequences at the 5′ ends, connecting sequences at the 3′ ends, and -GSGS- linkers in between DnaJB1-PKA$_{cat}$ and mCherry, which were Gibson assembled into HindIII- and XbaI-digested pcDNA3.1. mCherry-tagged DnaJB1-PKA$_{cat}^{K72H}$ was constructed by Gibson assembly of PCR products amplified from mCherry-tagged DnaJB1-PKA$_{cat}$. mTagBFP2-tagged DnaJB1-PKA$_{cat}$ and DnaJB1-PKA$_{cat}^{K72H}$ plasmids were constructed by Gibson assembly of PCR products amplified from mCherry-tagged DnaJB1-PKA$_{cat}$ or DnaJB1-PKA$_{cat}^{K72H}$, respectively, and from pBAD-mTagBFP2 (Subach et al., 2011). mCherry-tagged PKA$_{cat}^{G1A}$ was generated via Q5 site-directed mutagenesis (New England Biolabs). mCherry-tagged myristoylated-DnaJB1-PKA$_{cat}$, which contains only the first 8 amino acids of wild-type PKA$_{cat}$ (first 8 amino acids of Cα1, an isoform of PKA$_{cat}$, aligns with the consensus myristoylation sequence; Tillo et al., 2017; Udenwobele et al., 2017), was constructed by Gibson assembly of PCR products amplified from PKA$_{cat}$. mCherry-tagged DnaJB1^{H33Q}-PKA$_{cat}$ (Turnham et al., 2019) was constructed by Gibson assembly of PCR products amplified from mCherry-DnaJB1-PKA$_{cat}$. mCherry-myristoylated DnaJB1^{H33Q}-PKA$_{cat}$ was constructed by Gibson assembly of PCR products amplified from mCherry-tagged myristoylated DnaJB1-PKA$_{cat}$ using the same primers described above for the H33Q J-domain mutation.

Lentiviral constructs

pLenti backbone versions of RIα mutants tagged with EGFP were constructed by Gibson assembly of PCR products amplified from pLenti-puro (Guan et al., 2011) (gift of Ie-Ming Shih, Addgene plasmid #39481) and the respective pcDNA3.1 versions of RIα mutants.

Construct to purify superfolder green fluorescent protein

sfGFP in pRSET B was constructed by Gibson assembly of PCR products amplified from pEvolvR-enCas9-PolI3M-TBD (Halperin et al., 2018) (gift from John Dueber & David Schaffer, Addgene plasmid #113077) to amplify sfGFP and from pRSET B (Invitrogen) to amplify the pRSET B backbone.

Disorder and charge predictions of RIα

Disorder of full-length human RIα was predicted using PONDR (http://www.pondr.com/), which predicted that residues 63-105 and 264-320 are intrinsically disordered regions. The single-amino-acid and average (sliding window of 10 AA) charge distributions along the primary sequence were analyzed using EMBOSS (http://www.bioinformatics.nl/cgi-bin/emboss/charge), which predicted various regions to have high charge imbalance, such as the highly positively charged region of residues 81-96.

Cell counting to measure cell proliferation

MEF and AML12 stable cell lines were seeded in 6-wells plates at 10,000 cells/well. Cell numbers were quantified using a Countess II cell counter (Life Technologies) each day for 7 days.

BrdU staining to measure cell proliferation

MEF and AML12 stable cell lines were seeded on 35-mm glass-bottomed dishes at 10,000 cells/dish. At 48 h after plating, cells were treated with 10 μM BrdU (Invitrogen) for 4 h. Cells were washed twice with PBS and fixed with 3.7% formaldehyde in PBS. MEF and AML12 cells were imaged following application of standard immunofluorescence protocols: Triton X-100 permeabilization, 1 N and 2 N HCl addition, anti-BrdU primary antibody addition (1:100, Invitrogen), anti-mouse Alexa Fluor 647 (1:1000, Invitrogen), and 100 ng mL^{-1} DAPI nuclear staining.

Soft agar colony formation assay to assess cell transformation

Soft agar colony formation assays were performed as described previously (Borowicz et al., 2014). Briefly, 6-well plates were prepared containing 0.5% Noble Agar (Thermo Fisher) and 2X concentration of the respective cell media. After the agar solidified, 0.3% Noble Agar containing 5000 cells was applied on top of the 0.5% Noble Agar layer. MEFs and AML12 cells in soft agar were cultured in a 5% CO_2 incubator for several weeks with 200 μL of the respective culture media added on top of the gel twice per week. Visible colonies appeared after 3 (MEFs) to 4 weeks (AML12 cells) and were photographed using a Canon EOS 5D Mark III DSLR camera (Canon USA).

Protein purification

Recombinant RIα and RIIβ were purified as described previously (Bastidas et al., 2012; Bruystens et al., 2014) with slight modifications. Constructs were transformed into *Escherichia coli* BL21 (DE3) cells and inoculated in LB media with 100 μg mL^{-1} ampicillin. Cultures were induced at OD_{600} = 0.6-0.8. After 16 h of expression under 0.5 mM IPTG at 16°C, the cell pellets were collected and then re-suspended and lysed in lysis buffer (20 mM MES, pH 6.5, 100 mM NaCl, 2 mM EDTA, 2 mM EGTA, and 5 mM DTT plus protease inhibitors and 10 μM 3-isobutyl-1-methylxanthine (IBMX)). The supernatant was collected after high-speed centrifugation (13,000 rpm, 1 h) and incubated overnight with cAMP-resin at 4°C. After centrifugation (3,000 rpm, 10 min) and removal of the supernatant, the resin was then washed sequentially with lysis buffer, wash buffer (20 mM MES, pH 6.5, 600 mM NaCl, 2 mM EDTA, 2 mM EGTA, and 5 mM DTT), and lysis buffer again. The proteins were eluted using elution buffer (20 mM MES, pH 5.5, 100 mM NaCl, 30 mM cGMP, 2 mM EDTA, 2 mM EGTA, and 5 mM DTT). The eluted proteins were then concentrated and further purified on an S-200 gel filtration column in 50 mM MES, pH 5.8, 200 mM NaCl, and 5 mM DTT.

PKA_{cat} and DnaJB1-PKA_{cat} were each generated previously (Lu et al., 2019). The constructs were transformed into Rosetta pLysS (DE3) cells and inoculated in LB media with 50 μg mL^{-1} kanamycin. Cultures were induced at OD_{600} = 0.6-0.8. After 16 h of expression under 0.5 mM IPTG at 18°C, the pellets were collected and then re-suspended and lysed in lysis buffer (20 mM Tris-Cl, pH 8.0, 300 mM NaCl, and 5 mM β-mercaptoethanol (BME)). The supernatant was collected after high-speed centrifugation (13,000 rpm, 1 h) and then passed through Ni-resin. The resin was then washed with 3 column volumes (CVs) of wash buffer (20 mM Tris-Cl, pH 8.0, 300 mM NaCl, 10 mM imidazole, and 5 mM BME), and the proteins were eluted by adding 3 CVs of elution buffer (20 mM Tris-Cl, pH 8.0, 300 mM NaCl, 500 mM imidazole, and 5 mM BME). The eluent was collected and supplemented with His_6-tagged Ulp1 (Guerrero et al., 2015) (gift of Hideo Iwai, Addgene plasmid #64697), Ubiquitin-like-specific protease 1 (molar ratio SUMO-PKA_{cat} or SUMO-DnaJB1-PKA_{cat}:Ulp1 = 200:1). The solution was dialyzed (20 mM Tris-Cl, pH 8.0, 300 mM NaCl, and 5 mM BME) overnight at 4°C. The cleaved tag, His_6-tagged Ulp1, and uncleaved protein were removed by passing the solution back through the Ni-resin. After collection of the flow-through, the proteins were further purified by S-75 gel filtration in 20 mM MES, pH 6.5, 300 mM NaCl, and 5 mM BME.

To purify EGFP-PKA_{cat}, we used pET-His_6-EGFP-PKA_{cat}, which was constructed previously (Lu et al., 2019) and fuses EGFP to His_6 with a -GSS- linker and EGFP to PKA_{cat} with a -GSAGSAAGSGEF- linker. The plasmid was transformed into Rosetta pLysS

(DE3) cells and inoculated in LB media with 50 μg mL^{-1} kanamycin. Cultures were induced at OD_{600} = 0.6-0.8. After 16 h of expression under 0.5 mM IPTG at 18°C, the pellets were collected, re-suspended, and lysed in lysis buffer (20 mM Tris-Cl, pH 8.0, 300 mM NaCl, and 5 mM BME). The supernatant was collected after high-speed centrifugation (13,000 rpm, 1 h) and then passed through Ni-resin. The resin was then washed with 3 CVs of wash buffer (20 mM Tris-Cl, pH 8.0, 300 mM NaCl, 10 mM imidazole, and 5 mM BME), and proteins were eluted by adding 3 CVs of each elution buffer (20 mM Tris-Cl, pH 8.0, 300 mM NaCl, 50-500 mM imidazole, and 5 mM BME). After collection of the eluent, the protein was further purified via S-75 gel filtration in 20 mM MES, pH 6.5, 300 mM NaCl, 5 mM BME.

After purification, all aforementioned proteins were dialyzed into liquid droplet preparation buffer (150 mM KCl, 1 mM $MgCl_2$, 20 mM HEPES, pH 7.0, 1 mM EGTA, 1 mM DTT, 0.5 mM ATP, final pH 7.0) and concentrated using Amicon Ultra-15 centrifugal filters (Millipore). Protein concentrations were measured using the Pierce BCA protein assay kit (Thermo Fisher).

To purify sfGFP, the pRSET B sfGFP construct was transformed into *Escherichia coli* BL21 (DE3) cells and inoculated in LB media with 100 μg mL^{-1} ampicillin. Cultures were induced at OD_{600} = 0.6-1.0. After 6 h of expression under 0.5 mM IPTG at 37°C, the cell pellets were collected, re-suspended in lysis buffer (50 mM Tris, pH 7.4, 300 mM NaCl) containing 1 mM PMSF and Complete EDTA-free Protease Inhibitor Cocktail (Roche), and lysed by sonication. Following centrifugation at 25,000 × *g* for 30 min at 4°C, the clarified lysate was loaded onto an Ni-NTA column, washed with wash buffer (50 mM Tris, pH 7.4, 300 mM NaCl, 10 mM imidazole), and then eluted using an imidazole gradient (20-200 mM in lysis buffer). The eluted proteins were then concentrated, and the sfGFP protein concentration was measured via BCA assay and absorbance.

In vitro liquid droplet assays

All liquid droplet formation assays were performed in 150 mM KCl (unless specified), 5 mM $MgCl_2$, 10 μM cAMP (as indicated), 20 mM HEPES, pH 7.0, 1 mM EGTA, 1 mM DTT, 0.5 mM ATP, and 100 mg/ml Polyethylene Glycol 4000 (unless specified). Purified proteins were incubated at different stoichiometries and at various concentrations at room temperature for 1 h and imaged under DIC and/or fluorescence microscopy.

Fluorescent protein intensity calibration to measure RIα concentrations

Puncta RIα concentrations were estimated based on calibration of fluorescent protein intensity on the same imaging system used to generate the data shown in Figures 1A, 1B, 2, 3, 4, 5, S1, S2, S3, S4, and S5. Briefly, known concentrations of purified sfGFP were loaded in glass capilary tubes and imaged under the same illumination conditions used for live-cell imaging experiments. The resulting intensity images were used to construct a standard curve and calculate a calibration constant (i.e., number of sfGFP molecules per camera count) for the system. Using this value, we then estimated the RIα concentration in each fluorescent puncta in each cell based on the measured area and the mean intensity value, assuming spherical puncta.

Fluorescence recovery after photobleaching

Cells were imaged using a Nikon A1R HD confocal with a four-line (405 nm, 488 nm, 561 nm, and 640 nm) LUN-V laser engine and DU4 detector using bandpass and long-pass filters for each channel (450/50, 525/50, 595/50 and 700/75) mounted on a Nikon Ti2 using an Apo 100x 1.49 NA objective and operated using NIS Elements software. Image stacks were acquired in Galvano mode with unidirectional scanning with a 488 nm laser at 1.5% power with a frame size of 512 × 512 at scan zoom, 1 frame per second (fps), and 97.1 μm pinhole size. Small regions of interest (ROIs) for stimulation were drawn over the punctate structures and in the cytosol. The total FRAP series contained 3 images before bleaching (obtained at 2 s intervals), 2 cycles of ROI bleaching with the 488 nm laser at 100% laser power (5 frames at 1 fps), and 2 min of continuous acquisition to monitor fluorescence recovery.

Time-lapse epifluorescence imaging

Cells were washed twice with HBSS and subsequently imaged in HBSS in the dark at 37°C. Forskolin (Fsk; Calbiochem), 3-isobutyl-1-methylxanthine (IBMX; Sigma), rolipram (Rol; Alexis), myristoylated PKI 14–22 amide (Myr-PKI; Tocris), isoproterenol (Iso; Sigma), and 1,6-hexanediol (Hex; Sigma-Aldrich) were added as indicated. Epifluorescence imaging was performed either on a Zeiss Axiovert 200M microscope (Carl Zeiss) equipped with a xenon lamp, a 40x/1.3 NA objective and a cooled CCD or on a Zeiss AxioObserver Z1 microscope (Carl Zeiss) equipped with a 40x/1.3 NA objective and a Photometrics Evolve 512 EMCCD (Photometrics), both controlled by METAFLUOR 7.7 software (Molecular Devices). For the Zeiss Axiovert 200M, the following excitation/emission filter combinations (center/bandwidth in nm) were used: BFP - EX380/10, EM475/25; CFP - EX420/20, EM475/25; GFP - EX480/30, EM535/45; YFP - EX495/10, EM535/25; RFP - EX568/55, EM653/95; CFP/YFPFRET - EX420/20, EM535/25; GFP/RFPFRET - EX480/30, EM653/95. For the Zeiss AxioObserver Z1, the following excitation/emission filter combinations were used: GFP - EM480/30, EX535/45. All filter sets were alternated using a Lambda 10-2 filter-changer (Sutter Instruments). Exposure times were 50 (for acceptor direct channel) and 500 ms (for all other channels), with the EM gain set to 20 for the AxioObserver Z1 microscope, and images were acquired every 30 s. All epifluorescence experiments were subsequently analyzed using METAFLUOR 7.7 software. DIC images were acquired on the Zeiss Axiovert 200M microscope. Brightfield images were acquired on an eVos FL cell imaging system (Thermo Fisher).

QUANTIFICATION AND STATISTICAL ANALYSIS

FRET biosensor analysis

Raw fluorescence images were corrected by subtracting the background fluorescence intensity of a cell-free region from the emission intensities of biosensor-expressing cells. Green/red, red/green, or cyan/yellow emission ratios were then calculated at each time point (R). For some curves, the resulting time courses were normalized by dividing the emission ratio at each time point by the basal ratio value at time zero (R/R_0), which was defined as the emission ratio at the time point immediately preceding drug addition (R_0). Normalized-to-time-zero ratio changes (R/R_0) from drug stimulation ($\Delta R/R_0$ (drug)) were reported for some of the bar graphs and were calculated as $(R_{drug} - R_0)/R_{0,}$ where R_{drug} is the emission ratio at the last time point after the corresponding drug addition. For PDE4D2$_{cat}$-ICUE4 curves, the resulting time courses were normalized to the maximum ratio change ($\Delta R/\Delta R_{max}$) by calculating $(R - R_0)/(R_{max} - R_0)$, where R_{max} is the maximum emission ratio value recorded after all stimulations. Graphs were plotted using GraphPad Prism 8 (GraphPad).

Quantification of cellular puncta

For analysis of puncta number, cell images were individually thresholded and underwent particle analysis with circularity and size cutoffs in ImageJ.

Calculations for the apparent diffusivity of cAMP

The circular FRAP regions were saved and the radius (r) was calculated from the area. Time-to-half maximum values ($t_{1/2}$) were acquired from ImageJ data processing tools. Since the FRAP regions were circular, the apparent diffusivity (D_{app}) is calculated from the following equation (Kang et al., 2012):

$$D_{app} = 0.224\frac{r^2}{t_{1/2}}$$

Statistics and reproducibility

Statistical analyses were performed in GraphPad Prism 8 (GraphPad). All data were assessed for normality. For normally distributed data, pairwise comparisons were performed using unpaired two-tailed Student's t tests, with Welch's correction for unequal variances used as indicated. Comparisons between three or more groups were performed using ordinary one-way analysis of variance (ANOVA). For data that were not normally distributed, pairwise comparisons were performed using the Mann-Whitney U test, and comparisons between multiple groups were performed using the Kruskal-Wallis test. Statistical significance was set at $p < 0.05$. Average time courses shown in Figures 1C; 3B, 3C, 3E, 3G, and 3H (curves); 4B–4D (curves); 5E (curves); S1A; S3A, S3B, S3D, and S3F (curves); and S4B, S4D, S4E, and S4H–S4K (curves) are representative of at least 3 independently repeated experiments. Average time courses and bar graphs shown in Figures 1D; 2B and 2F; 3B–3H (bar graphs); 4B–4D (bar graphs); 5B–5D, 5E (bar graphs), and 5F–5H; S1C–S1E; S2B–S2H; S3C, S3D (bar graph), S3F, and S3G; S4B (bar graph), S4F–S4J (bar graphs), and S4L; and S5E–S5G combined datasets from at least 3 independent experiments, unless otherwise stated.

Throughout the paper, ****$p < 0.0001$ and ††††$p < 0.0001$. Kruskal-Wallis test followed by Dunn's multiple comparisons test was performed for Figures 2B (* versus wild-type RIα and † versus Δ(D/D+linker)), 5D (†, versus the corresponding DnaJB1-PKA$_{cat}$ + RIα column), S2B (versus wild-type RIα), and S5F (versus WT). Unpaired two-tailed Student t tests were performed for Figures 3D, 3F, 5E, S3D, S4B, S4F, and S4L, and Welch's correction was applied for Figures 3B, 3C, 3E, 3G, 3H, 4B–4D, 5B, and S4H–S4J. Unpaired two-tailed Mann-Whitney U-tests were performed for Figures 5D (*, –Fsk versus +Fsk), S2D, and S2F. Ordinary one-way ANOVA followed by Dunnett's multiple comparisons test was performed for Figures 5G, 5H, and S5G (all versus WT) and followed by Tukey's multiple comparisons test for Figure S4G. A one-sample t test versus a hypothetical value of 1 was performed for Figure S5E.

CellPress

Supplemental Figures

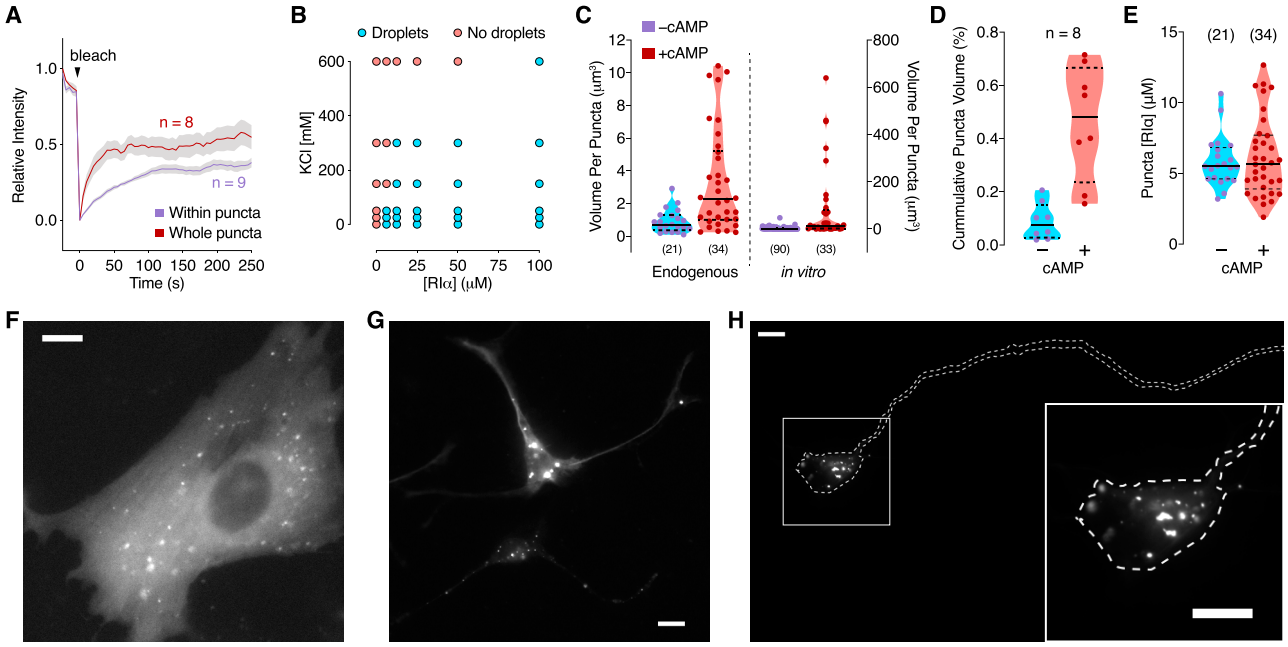

Figure S1. Additional Characterization of RIα Phase-Separated Bodies, Related to Figure 1

(A) FRAP of a region within an RIα puncta (blue curve) compared with an entire RIα puncta (red curve) in HEK293T cells transfected with RIα-EGFP. Curves show average time course of normalized fluorescence intensity. Solid lines indicate the mean; shaded areas, SEM.

(B) Representative *in vitro* phase diagram of RIα liquid droplet formation at varying concentrations of KCl. Each condition was assessed at least twice.

(C–E) Average size of (C), percent volume occupied by (D), and RIα concentrations inside RIα droplets (E) in 293-RIα cells transfected with GFP_{1-10} (endogenous) or *in vitro* RIα droplets (*in vitro*) (50 μM RIα + 12.5 μM PKA_{cat}). Analyses were performed before and after 50 μM Fsk stimulation (endogenous) or 10 μM cAMP addition (*in vitro*) (endogenous: −cAMP: n = 21 puncta from 8 cells, +cAMP: n = 34 puncta from 8 cells; *in vitro*: −cAMP: 93 droplets, +cAMP: 34 droplets). Violin plots show the median and quartiles as solid and dashed lines, respectively.

(F–H) RIα phase separation occurs in various cell types. Representative fluorescence images of EGFP-RIα-expressing (F) neonatal rat ventricular myocytes, (G) astrocytes, and (H) dissociated primary embryonic rat hippocampal neurons grown for 3 days *in vitro* (outline indicates cell shape; inset, zoomed image) showing RIα puncta formation. Scale bars, 10 μm.

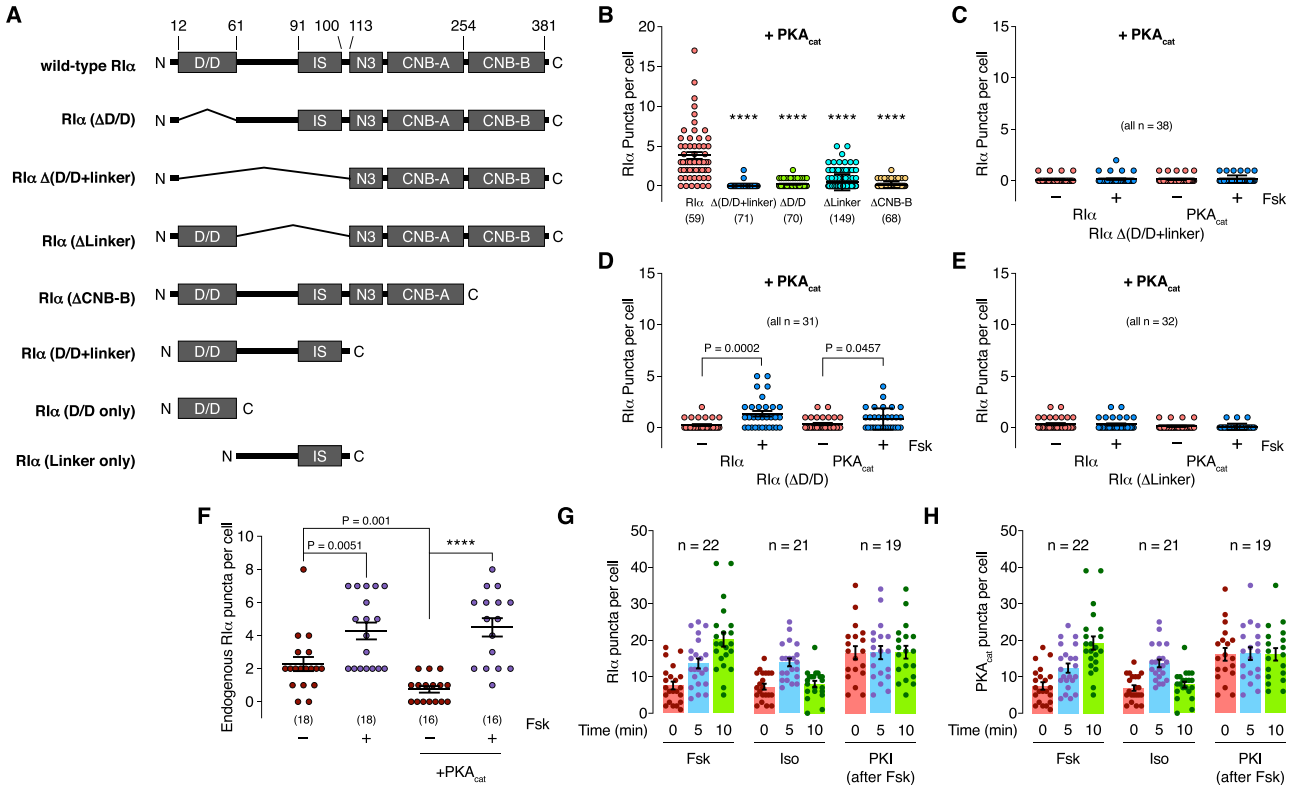

Figure S2. RIα Phase Separation Requires the D/D Domain and Linker Region and Is Regulated by PKA_{cat} and cAMP, Related to Figure 2

(A) Domain structure of RIα (D/D: docking/dimerization domain, IS: inhibitory sequence, CNB-A: cAMP binding domain A, N3, a motif at the beginning of CNB-A; CNB-B: cAMP binding domain B) and the various truncation mutants used in this study.

(B) Comparison of the number of basal RIα puncta per cell in cells expressing PKA_{cat} plus either wild-type RIα or various RIα mutants. Deletion of either the D/D domain or linker region greatly reduced the number of RIα puncta per cell.

(C–E) Comparison of the number of basal and Fsk-stimulated RIα puncta in HEK293T cells expressing mCherry-tagged PKA_{cat} plus EGFP-tagged $RI\alpha_{\Delta D/D+Linker}$ (C), $RI\alpha_{\Delta D/D}$ (D), or $RI\alpha_{\Delta Linker}$ (E) and stimulated with 50 μM Forskolin (Fsk).

(F) Comparison of the number of RIα puncta per cell in 293-RIα cells with or without PKA_{cat} overexpression and stimulated with 50 μM Fsk. Overexpressing PKA_{cat} decreases the basal RIα puncta number.

(G and H) Comparison of the number of RIα (G) and PKA_{cat} puncta (H) per cell in HEK293T cells expressing EGFP-RIα and mCherry-PKA_{cat} and treated with 50 μM Fsk, 10 μM isoproterenol (Iso), or 20 μM myrisotylated-PKI (Myr-PKI) 20 min after 50 μM Fsk addition. Fsk and Iso dynamically increase the numbers of both RIα and PKA_{cat} puncta while Myr-PKI treatment following Fsk stimulation has no effect.

Horizontal lines in (B)–(F) indicate mean ± SEM. Bars in (G) and (H) indicate mean ± SEM. ****$p < 0.0001$ versus RIα; Kruskal-Wallis test followed by Dunn's multiple-comparisons test.

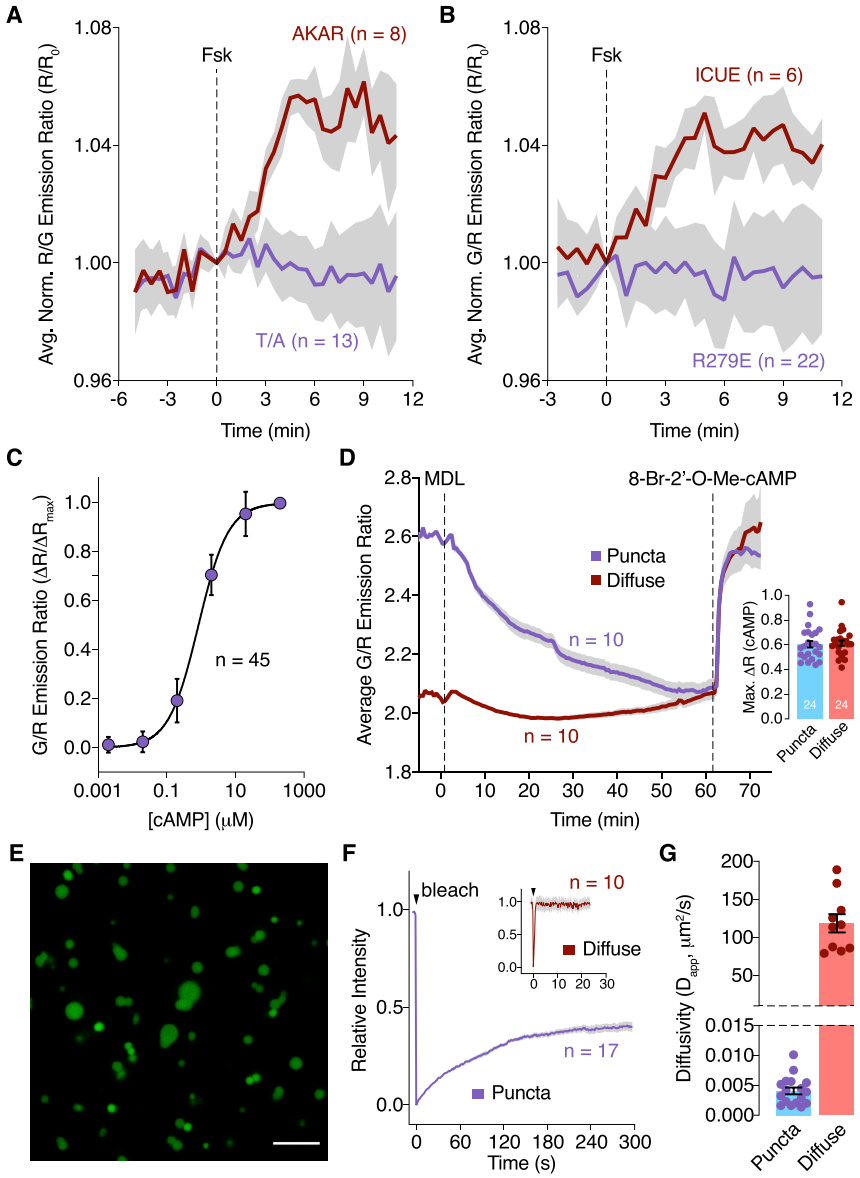

Figure S3. Additional Characterization of FluoSTEP-AKAR and FluoSTEP-ICUE, Related to Figure 3

(A and B) Testing the specificity of FluoSTEP-AKAR and FluoSTEP-ICUE. Representative whole-cell average time courses showing (A) the red/green (R/G) emission ratio of either FluoSTEP-AKAR (red curve) or FluoSTEP-AKAR T/A (blue curve) or (B) the green/red (G/R) emission ratio of either FluoSTEP-ICUE (red curve) or FluoSTEP-ICUE R279E (blue curve) in 293-RIα cells stimulated with 50 μM Fsk.

(C) Characterizing the dose-response behavior of G/R-ICUE. HEK293T cells were pretreated with 100 μM MDL-12330A followed by the indicated concentrations of 8-Br-2′-O-Me-cAMP-AM.

(D) Targeting to puncta does not affect the G/R-ICUE response. Left: Representative average time courses of G/R emission ratio changes in HEK293T cells transfected with RIα-G/R-ICUE and stimulated with 100 μM MDL-12330A (MDL) followed by 200 μM 8-Br-2′-O-Me-cAMP-AM (n = 10 puncta and 10 diffuse regions from 10 cells). RIα puncta regions (blue curve) and non-puncta regions (red curve) were analyzed separately. Right: Maximum raw emission ratio changes upon 8-Br-2′-O-Me-cAMP-AM treatment (n = 24 puncta and 24 diffuse regions from 24 cells).

(E) When added to 50 μM purified RIα, 10 μM dye-labeled cAMP analog (8-Φ-450-cAMP) preferentially localized within RIα droplets, with 99% ± 0.33% of cAMP in the droplets. Scale bar, 10 μm.

(F) cAMP FRAP experiments using dye-labeled cAMP reveal much slower fluorescence recovery within RIα droplets (Puncta) versus when cAMP is alone in solution (Diffuse; inset).

(G) Apparent diffusion coefficients of puncta-localized or diffuse cAMP calculated from FRAP experiments.

Solid lines in (A), (B), (D), and (F) indicate the mean; shaded areas, SEM. Error bars in (C), (D) and (G) depict mean ± SEM.

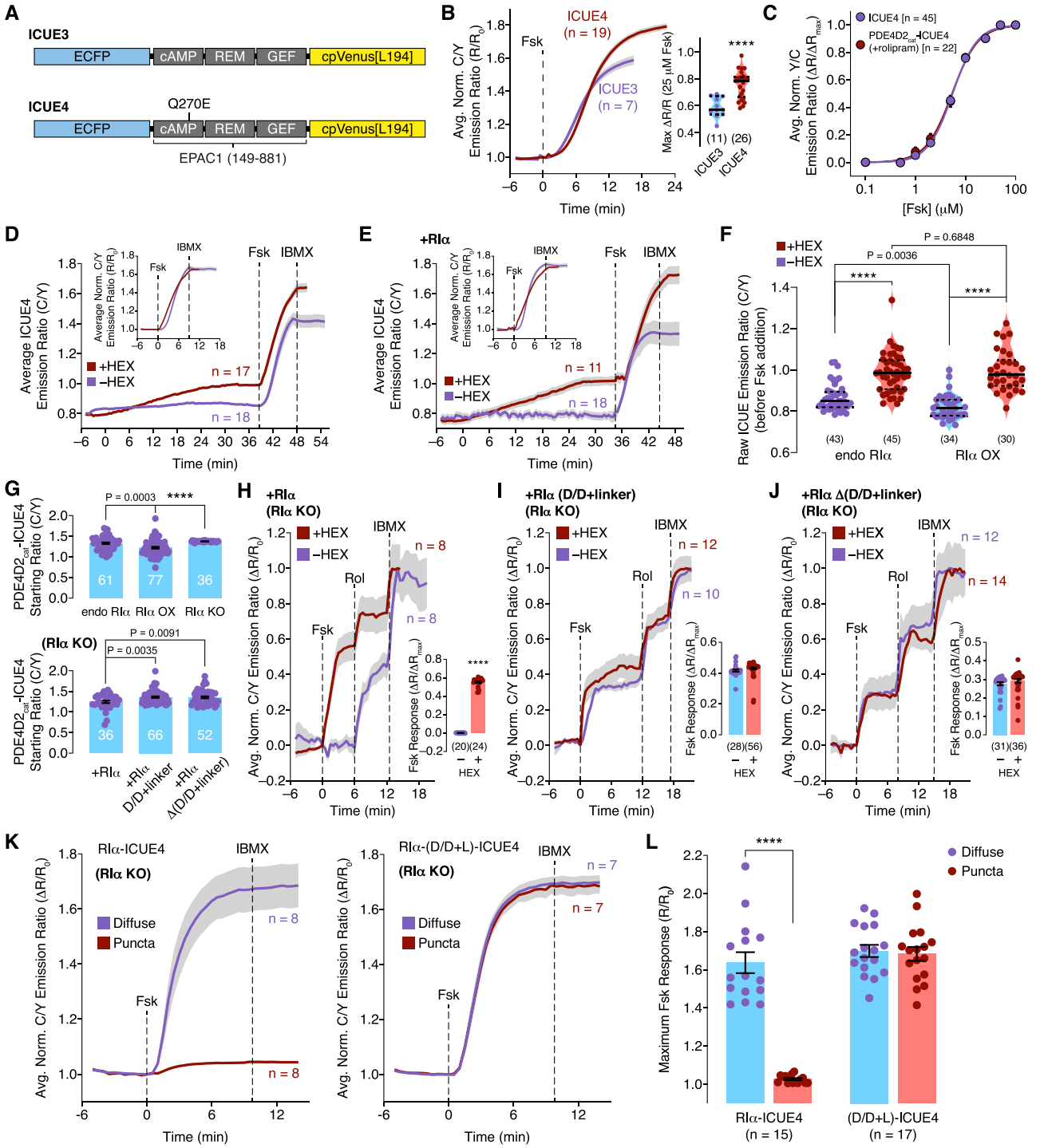

Figure S4. RIα Phase Separation Plays a Crucial Role in Maintaining PDE-Mediated cAMP Compartmentation, Related to Figure 4

(A and B) Characterizing the improved cAMP sensor ICUE4. (A) Domain structures of ICUE3 and ICUE4. (B) Representative average time courses of the cyan/yellow (C/Y) emission ratio in HEK293T cells expressing either ICUE3 (blue curve) or ICUE4 (red curve) and stimulated with 25 μM Fsk. Inset: Comparison of the maximum C/Y emission ratio responses of ICUE3 and ICUE4 after 25 μM Fsk stimulation. ****$p < 0.0001$; unpaired-two-tailed Student's t test.

(C) PDE4D2$_{cat}$ tethering does not affect the ICUE4 response. HEK293T cells expressing ICUE4 (blue curve) or PDE4D2$_{cat}$-ICUE4 (red curve) were stimulated with different doses of forskolin (Fsk) in the absence (ICUE4) or presence (PDE4D2-ICUE4) of the PDE4 inhibitor rolipram. Points indicate mean ± SEM.

(D and E) Representative average time courses of the C/Y emission ratio in HEK293T cells expressing ICUE4 (D) or ICUE4 plus mRuby2-RIα (E) with (red curve) and without (blue curve) 1,6-hexanediol treatment (added at t = 0 in the red curve) followed by 50 μM Fsk and then 100 μM IBMX. Hexanediol treatment induces a

(legend continued on next page)

gradual increase in the ICUE4 C/Y emission ratio compared with control (blue curve) but has little effect on the maximum stimulated ICUE4 responses (see insets showing responses normalized to Fsk addition).

(F) Comparison of the raw C/Y emission ratio of cytosolic ICUE4 immediately prior to Fsk stimulation with and without hexanediol treatment in HEK293T cells with endogenously expressed RIα (endo RIα) or RIα overexpression (RIα OX). ****$p < 0.0001$; unpaired two-tailed Student's t test.

(G) Top: Comparison of the raw initial C/Y emission ratios of PDE4D2$_{cat}$-ICUE4 in HEK293T cells with endogenously expressed RIα (endo RIα), RIα overexpression (RIα OX), or RIα knockout (RIα KO). Bottom: Comparison of the raw initial C/Y emission ratios of PDE4D2$_{cat}$-ICUE4 in RIα knockout HEK293T cells expressing wild-type RIα, RIα$_{D/D+Linker}$, or RIα$_{\Delta D/D+Linker}$. ****$p < 0.0001$; ordinary one-way ANOVA followed by Tukey's multiple comparisons test.

(H–J) Left: Representative average time courses of the C/Y emission ratio (normalized to max) of PDE4D2$_{cat}$-ICUE4-transfected RIα KO HEK293T cells co-expressing mRuby2-RIα (+RIα) (H), mRuby2-RIα$_{D/D+Linker}$ (+RIα$_{D/D+Linker}$) (I), or mRuby2-RIα$_{\Delta D/D+Linker}$ (+RIα$_{\Delta D/D+Linker}$) (J) with (red curve) and without (blue curve) hexanediol pretreatment and stimulation with 50 μM Fsk, 1 μM rolipram (Rol), and 100 μM IBMX. Right: Bar graphs showing the average normalized-to-max PDE4D2$_{cat}$-ICUE4 (C/Y) emission ratio after Fsk stimulation for each condition. ****$p < 0.0001$; unpaired two-tailed Student's t test with Welch's correction.

(K and L) Additional examination of cAMP levels inside and outside RIα droplets. RIα KO HEK293T cells expressing ICUE4 tethered to either full-length RIα (RIα-ICUE4) (left) or RIα$_{D/D+Linker}$ (RIα$_{D/D+Linker}$-ICUE4) (right), which phase separates but does not bind to cAMP, were stimulated with 50 μM Fsk and then 100 μM IBMX. RIα puncta (red curve) and diffuse regions (blue curve) were analyzed separately. Representative average time courses of C/Y emission ratio (K) and maximum Fsk-stimulated ratio changes (L) are shown. Consistent with FluoSTEP imaging, these results suggest that cAMP levels are substantially higher in RIα droplets, which depends on the cAMP-binding capabilities of RIα. ****$p < 0.0001$; unpaired two-tailed Student's t test.

Solid lines in (B), (D), (E), and (H)-(K) indicate the mean; shaded areas, SEM. Error bars in (C), (G), (H)-(J), and (L) depict mean ± SEM. Violin plots in (B) and (F) show the median and quartiles as solid and dashed lines, respectively.

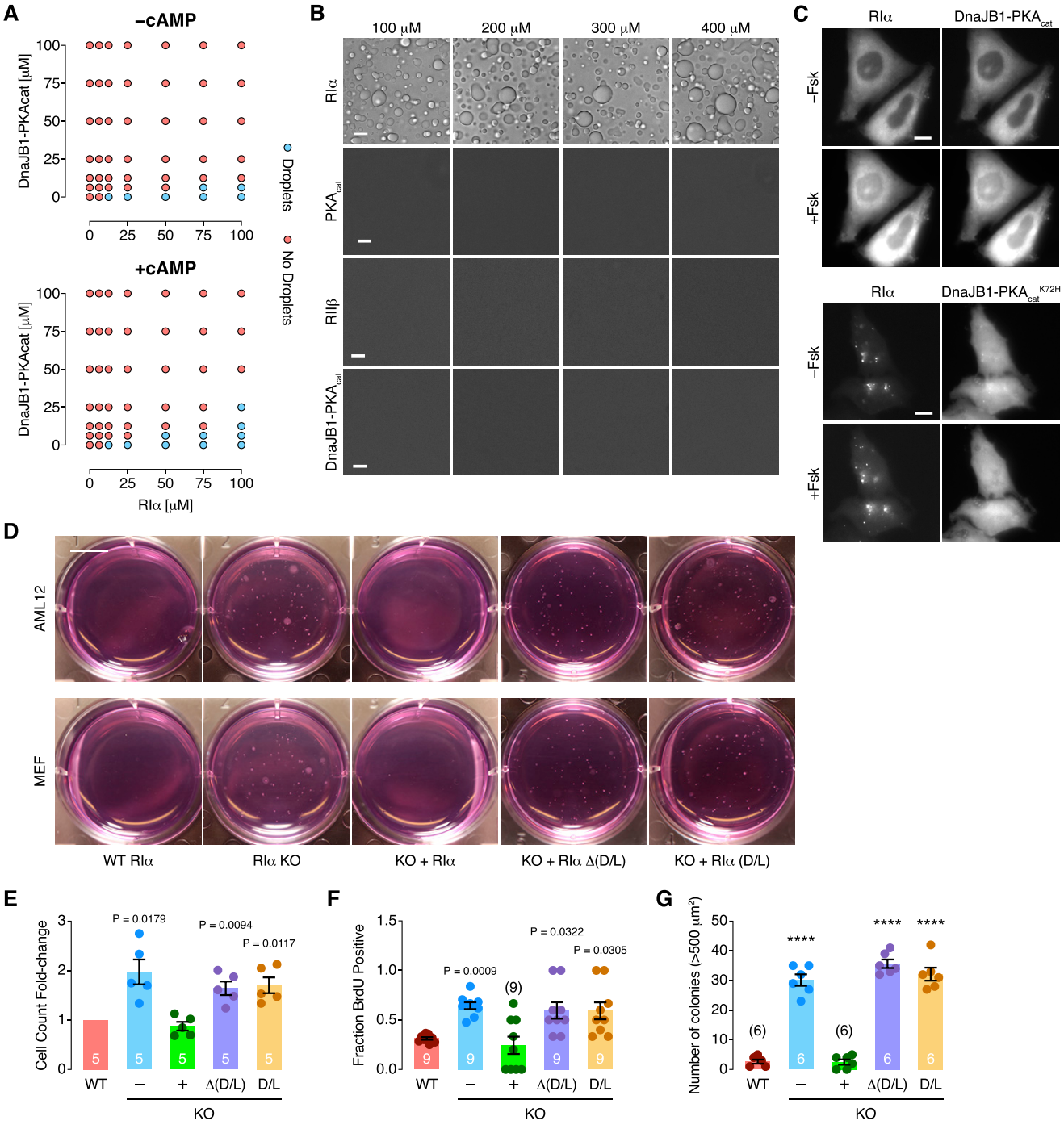

Figure S5. DnaJB1-PKA$_{cat}$ Abolishes Rlα Phase Separation, and Loss of Rlα Phase Separation Leads to Tumorigenic Phenotypes, Related to Figure 5

(A) Representative *in vitro* phase diagram of Rlα liquid droplet formation as a function of Rlα and DnaJB1-PKA$_{cat}$ concentration in the absence (top) or presence (bottom) of 10 μM cAMP, showing that DnaJB1-PKA$_{cat}$ disrupts Rlα phase separation. Each condition was assessed at least twice.

(B) Purified Rlα, PKA$_{cat}$, PKA type II regulatory subunit (RIIβ), or DnaJB1-PKA$_{cat}$ at the indicated concentrations were incubated in liquid droplet buffer to assess *in vitro* liquid droplet formation. Only Rlα showed droplet formation. Scale bars, 10 μm.

(C) DnaJB1-PKA$_{cat}$ disrupts Rlα puncta formation in cells. Representative fluorescence images of HEK293T cells transfected with EGFP-Rlα and either mTagBFP2-tagged DnaJB1-PKA$_{cat}$ (upper images) or DnaJB1-PKA$_{cat}^{K72H}$ (JB1-Cat^{K72H}, lower images) before (t = 0 min, top) or after (t = 20 min; bottom) 50 μM Fsk addition. Scale bars, 10 μm.

(legend continued on next page)

(D) Representative photographs of AML12 cell (top) or mouse embryonic fibroblast (MEF) colonies (bottom) embedded in soft-agar in 6-well plates for each condition. Mutations that disrupt RIα phase separation also promote anchorage independent cell growth. Scale bar, 10 mm.
(E–G) Loss of RIα phase separation or cAMP sequestration promotes tumorigenic phenotypes in MEFs. RIα null cells were transfected with $RI\alpha_{D/D+Linker}$, which permits RIα phase separation but lacks cAMP binding, or $RI\alpha_{\Delta(D/D+Linker)}$, which retains cAMP binding but lacks phase separation. (E) Average fold-change in cell count for MEFs under different conditions after 1 week of growth. Data were analyzed using the Kruskal-Wallis test followed by Dunn's multiple comparisons test. (F) Average percentage of BrdU+ MEFs. Data were analyzed using the Kruskal-Wallis test followed by Dunn's multiple comparisons test (versus WT). (G) Average number of colonies larger than 500 μm^2 grown in soft agar. ****$p < 0.0001$; ordinary one-way ANOVA followed by Dunnett's multiple comparisons test. Bars in (E)–(G) indicate mean ± SEM.